DOI: 10.1002/ ((please add manuscript number))
Article type: Review

Miscellaneous and Perspicacious: Hybrid Halide Perovskite Materials Based Photodetectors and Sensors

*Xiaoyan Yu[1,2,3], Hoi Nok Tsao[4], and Peng Gao[1,2,3]**

1. X. Yu, Prof. P. Gao
CAS Key Laboratory of Design and Assembly of Functional Nanostructures and Fujian Provincial Key Laboratory of Nanomaterials, Fujian Institute of Research on the Structure of Matter, Chinese Academy of Sciences
Fuzhou 35002, China
E-mail: peng.gao@fjirsm.ac.cn
2. X. Yu, Prof. P. Gao
Laboratory of Advanced Functional Materials, Xiamen Institute of Rare Earth Materials Haixi Institute, Chinese Academy of Sciences
Xiamen 361021, China
3. X. Yu, Prof. P. Gao
University of Chinese Academy of Science
Beijing 100049, China
4. Prof. H. N Tsao
Natural Sciences and Science Education, National Institute of Education, Nanyang Technological University Singapore
Singapore 637616

Keywords: perovskites, photodetectors, sensors, imaging, sensitivity

Optoelectronic devices based on perovskite materials have shown significant improvement due to the direct and tunable bandgap, large absorption coefficients, broad absorption spectra, high carrier mobilities, and long carrier diffusion lengths. In addition to the excellent performance in solar cells, scientists have utilized perovskite materials for other optoelectronic applications as well. This review details the figure-of-merits and development of perovskite-based photodetectors, including UV to NIR detection and high energy particle sensing. Discussions are made depending on different device structures. Furthermore, we review gas, compounds, temperature, and pressure sensors based on perovskite materials.

Abbreviation List

BCP = 2,9-dimethyl-4,7-diphenyl-1,10-phenanthroline
c = the velocity of light in vacuum
D^* = specific detectivity
e = the electro charge
EQE = external quantum efficiency
E_i = internal quantum efficiency
FRET = fluorescence resonance energy transfer
FET = field-effect transistor
GFET = graphene field-effect transistor
h = Plank's constant
λ = the wavelength of the incident light
LDR = linear dynamic range
MSM = metal-semiconductor-metal
NEP = noise equivalent power
NIR = near-infrared
OAED = optically-active-but-electronically-dead
PLZT = $Pb_{0.92}La_{0.08}Zr_{0.52}Ti_{0.48}O_3$
PEN = poly[(9,9-bis(3'-(N,N-dimethylamino)propyl)-2,7-fluorene)-alt- 2,7-(9,9-dioctylfluoren
PVDF = poly(vinylidene fluoride)
PMMA = polymethyl methacrylate
RC = resistance-capacitance
SNR = signal to noise ratio
RDX = 1,3,5-trinitroperhydro-1,3,5-triazine
SWCNTs = single-wall carbon nanotubes
TNT = 2,4,6-trinitrotoluene
TNG = trinitroglycerin

1. Introduction

In 2009, Miyasaka and colleagues reported the novel $CH_3NH_3PbBr_3$ and $CH_3NH_3PbI_3$ for visible light conversion in photovoltaic cells and showed a power conversion efficiency of 3.8% for a $CH_3NH_3PbI_3$-based solar cell.[1,2] Up to now, the record efficiency of perovskite solar cells stands at 25.2% from KRICT&MIT.[3] So far, in terms of crystal structures, two main kinds of perovskites have been used in optoelectronics devices. The first kind is the typical three dimensional (3D) organometal trihalide perovskite, whose crystal structure are abbreviated as AMX_3 (A is an organic cation, e.g.$CH_3NH_3^+$, $HN=CHNH_3^+$; M is a metal cation, e.g., Sn^{2+}, Pb^{2+}; X is a halide anion, e.g., Cl^-, Br^-, I^-). In the 3D crystal framework, corner-sharing BX_6 octahedrons form the 3D network with the A cations situated in the cuboctahedral interstices.[4,5] The inorganic components of the halide perovskite provide the molecular backbone required by the carrier's ordered transmission and also provides the thermal and mechanical stability of the material. The organic components on the other hand facilitate film formation through the interaction of hydrogen bonds and function as templates.

Different from 3D perovskite, layer-structured 2D perovskite materials follow the $(RNH_3)_2(A_3)_{n-1}M_nX_{3n+1}$ structure, where R is an alkyl or aromatic moiety larger than A, and n is the number of inorganic layers between the organic chains.[6,7] Thus, when $n=\infty$, the structure converts to 3D perovskite. On the other hand, when n=1, the structure becomes a quantum well in which only one layer of AX_4^{2-}, separated by a layer of organic cations via weak van der Waals forces hold the adjacent layers. The inorganic components provide high carrier mobility and wide bandgap tunability. The organic components, being either large aliphatic or aromatic ammonium cations, can enhance hydrophobicity by preventing water molecules from penetrating and destroying the inorganic layers. Thus 2D perovskites demonstrated improved environmental stability against moisture.[8–10] Importantly, 2D perovskite crystals also showed unique optical properties such as deep blue emission and

strong excitonic effect due to strong light-matter interactions.[11] Furthermore, to solve the instability issue of hybrid perovskites under high-temperature and humid environments, scientists have prompted the development of all inorganic perovskites (e.g., $CsPbX_3$) by replacing the organic component with inorganic ions.[12]

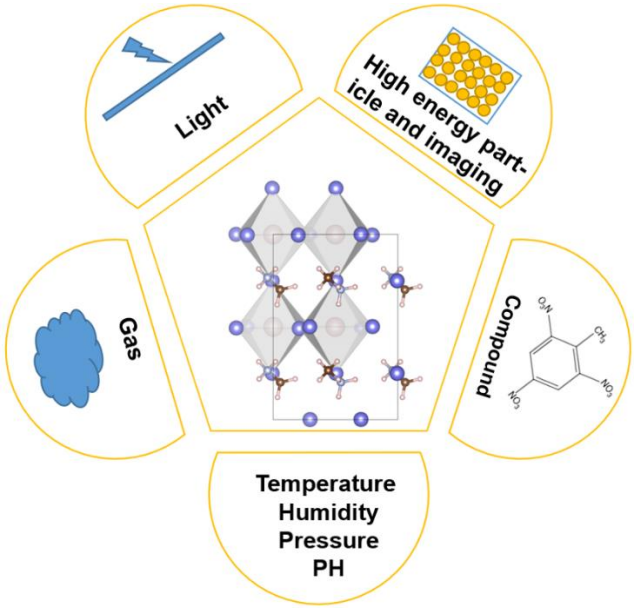

Figure 1. Various sensing and detecting devices employing perovskite materials.

Besides the rapid development of perovskite-based photovoltaics,[13–16] other perovskite related applications include light-emitting diodes (LED),[17–20] laser devices,[21–23] transistors,[24] thermoelectric generators,[25] photodetectors for UV-NIR photons,[26–29] and various sensors such as gas, chemical, and pressure.[30–33] In the field of perovskite devices, detectors and sensors have became very active areas of research beside photovoltaics and LEDs (**Figure 1**). This trend can be attributed to the favourable intrinsic properties of hybrid halide perovskites such as direct and tunable bandgaps with significant absorption coefficients, ultra-long charge carrier lifetimes/diffusion lengths, high carrier mobilities, low charge carrier recombination, broad absorption spectra, high external quantum efficiency (EQE) over the absorbing regions, and all-round chemical activity. [34–42] These extrodinary features endow perovskite based detectors (or sensors) with broad detection range (miscellaneous) and/or low

detection limit toward targets (perspicacious). Furthermore, compared to conventional rigid inorganic materials such as Si, InP, GaN, InGaAs, and InGaAsP used for detector applications, perovskite-based materials can be applied on flexible substrates to fabricate bendable devices with remarkable optical and electric performance.

The first hybrid organic-inorganic perovskite ($CH_3NH_3PbI_3$) photodetector was reported by Xia et al. in 2014. The device showed typical responsivity of 0.49 μ A W^{-1} and time response constant of 0.02s for both the rise and decay time, indicating that hybrid halide perovskites are promising light-harvesting materials for photodetectors.[43] Four years later, using the same perovskite ($CH_3NH_3PbI_3$), Lin et al. reported a high-performance detector with almost every notable figure-of-merit (responsivity of 5.6×10^8 A W^{-1}, detectivity of 2.8×10^{16} Jones, LDR of 92 dB), via a hybridized mechanism of photodiode and photoconductor.[44] The rapid improvement of device performance can be attributed to the continued progress in perovskite deposition techniques, together with a deepening in the understanding of perovskite crystallography as well as optimization of the device structures. Reviews on the preparation technology and morphology exist[45–48], while not much cross discussion was made about device structures.[49] In this review, we discuss and analyze the development of perovskite-based photodetectors (including high energy irradiation and visible light) in terms of different device structures with unique characteristics. In addition, other sensing devices for gas, compounds, temperature, pH value, humidity, and pressure over recent years are also reviewed.

2. Photodetectors

2.1. The key figure of merit

To evaluate photodetector performance, several figures of merit are of importance, such as the **linear dynamic range (LDR)** which highlights the linear association scales between the photocurrent and the light irradiance intensity. LDR can be calculated using Equation (1):

$$\mathrm{LDR}=20\log\frac{I_{upper}-I_0}{I_{lower}-I_0} \quad (1)$$

where I_{upper} is the current at which the detector response deviates from the straight line, I_{lower} is the lowest current in the linear range, and I_0 is the dark current. This equation reveals that at low dark currents, the photodetector performance improves due to a higher signal-to-noise ratio.[50] The lower limit of LDR is generally determined by noise or dark current, while the upper limit is mainly influenced by saturation effect or overload. Large LDR implies that the photodetector can detect both weak and strong light signals. In the case where the light intensity cannot be detected or converted precisely, the device may still work if its performance is well characterized.

The **photo-responsivity** is another critical parameter quantifying the efficiency of a photodetector's response to optical signals. Particularly, it refers to the net photocurrent generated by the device due to photon absorption under the incident light irradiation in unit time and is defined as

$$\mathrm{R}=\frac{I_{photo}}{P_{hv}S}=\frac{I_{illuminated}-I_0}{P_{hv}S} \quad (2)$$

where $I_{illuminated}$ is the photocurrent under illumination, P_{hv} is the irradiance of the incident light and *S* is the active area.[50]

For certain applications, the response time of the photodetector critically defines the response speed of the optical signals, including rise-time and fall- (or decay) time. Typically, upon light intensity alterations, the photocurrent does not immediately change due to the dynamic behavior of photo-generated carriers. Two types of response time exist to quantify this behaviour. One is the rise time (τ_r) defined as the time required for the photocurrent to rise to 90% of its stable state, whereas the fall time (τ_f) denotes the period needed for the photocurrent to drop to 10% of its stable state. These rise and fall times are utilized to

characterise the fast response of photodiodes, avalanche photodiodes, and photomultiplier tubes. In photocells, photoresistors and thermoelectric detectors for instance, τ_r and τ_f are 1-1/e (63%) and 1/e (37%) of their stable values, respectively. Another description is 3-dB bandwidth, which is defined as 0.5 times the modulation frequency of the photoresponse under continuous illumination. Among, the carrier transit time t_{tr} and RC time constants are the decisive factor. The higher the light response speed, the shorter the RC time constants, leading to improved photodetector sensitivity.

Not all incident photons can be absorbed to create free electron and hole pairs. Furthermore, due to charge recombination or trapping, not all photo-generated charge carriers can be collected to generate photocurrent.[51] The **external quantum efficiency (EQE)** describes this limitation and is defined by Equation (3):

$$E_e = \frac{Rhc}{e\lambda} \quad (3)$$

where h is the Plank's constant, c is the velocity of light in vacuum, e is the electric charge, and λ is the wavelength of the incident light.[28] The EQE gives an indication of photodetector sensitivity, with large EQE corresponding to high sensitivity. Another parameter of interest is the number of photo-generated carriers per absorbed photon, defined as **internal quantum efficiency (** E_i **)**, which can be expressed as Equation (4):

$$E_i = \frac{E_e}{total\ absorption} \quad (4)$$

Typically, EQE ranges between 0 and 1. However, there are situations where the EQE could be above 1 due to the gain defined by the ratio of measured current (i_a) and initial current (i_{in}) (Equation 5). High gain can maximize the sensitivity of photodetectors.

$$G = \frac{i_a}{i_{in}} \quad (5)$$

Since the responsivity of the photodetector does not follow a linear relationship with the intensity of the radiant energy in a wide range, it is impossible to extrapolate the signal to noise ratio (SNR) in the intense radiation from the weak radiation. Therefore, the **specific detectivity** (D^*) is a critical photodetector figure-of-merit and can be calculated by Equation (6):

$$D^* = \frac{(\mathrm{Sf})^{1/2}}{(R/i_n)} = \frac{R}{(2eI_0)^{\frac{1}{2}}} \quad (6)$$

where f is the electrical bandwidth and i_n is the shot noise. Detectivity can accurately reflect the capacity limit of a photodetector in detecting weak light. The higher the D^*, the better the performance.

Finally, the noise equivalent power (NEP) is also vital for photodetectors and denotes the minimum impinging optical power a detector can distinguish from the noise, and can be expressed as Equation (7):

$$\mathrm{NEP} = \frac{(\mathrm{Sf})^{1/2}}{D^*} = \frac{i_n}{R} \quad (7)$$

Photodetector noise can be classified into dark current noise, shot noise, and thermal noise. The dark current determines the minimum detectable light intensity. Therefore, reducing the dark current will improve the sensitivity of the photodetector. The shot noise, determined by $\mathrm{i_{n,\ s}} = \sqrt{2\mathrm{eI_dB}}$, occurs during the generation-recombination of photons. Another source of noise is thermal noise generated by the random motion of electrons, resulting in voltage fluctuations. The smaller the NEP is, the better the detector at detecting weak signals.

A summary of research works on perovskite-based photodetectors for UV-NIR light detection over recent years is listed in **Table 1**. These detectors are divided into three parts marked by different colors (red, yellow, green), representing metal-semiconductor-metal, photovoltaic, and field-effect transistor-type detectors, respectively.

Table 1. The device structure and performance of photodetectors based on perovskite light response materials*

Device structure	Responsivity (A W^{-1})	D^* (Jones)	LDR (dB)	Dark current (A)	Rise time (ms)	Fall time (ms)	Detect wavelength (nm)	Ref.
PET/Au/$CsPbBr_3$/Au	2.4×10^{-4}	10^{10}	/	4.8×10^{-8}	260	/	254(254-vis)	[12]
ITO/$MAPbBr_3$/ITO	Over 4000	Over 10^{13}	/	/	/	$<2.5\times10^{-2}$	520(375-550)	[52]
Ag/$CsPbBr_3$/Ag	6	/	/	4×10^{-9}	/	/	550(440-570)	[53]
Printed circuit board/ Au/glass/$CsBi_3I_{10}$/Au	21.8	1.93×10^{13}	/	2.38×10^{-13}	0.33	0.38	650(400-700)	[54]
Substrate/$CsPbBr_3$/ITO	118	8×10^{12}	/	7×10^{-11}	<40	<40	520(350-520)	[55]
PET/Au/$MAPbI_3$/ PDPP3T	2.55×10^{-2}	1.5×10^{10}	/	1.64×10^{-10}	/	/	650(365-937)	[56]
ITO/$MAPbI_3$/ITO	1.2	2.39×10^{12}	/	1.1×10^{-9}	<10	<10	630	[57]
PET/Au/$MAPbI_3$/ PMMA/Au	0.1	1.02×10^{12}	/	7×10^{-11}	0.3	0.4	650(400-800)	[58]
Substrate/$(C_6H_5CH_2CH_2NH_3)_2PbBr_4$ /Au	2.5×10^{-3}	1.55×10^{13}	/	10^{-13}	0.41	0.37	375(UV)	[59]
ITO/PET/PDMS/ITO/ PET/$MAPbI_3$	0.418	1.22×10^{13}	/	/	<80	<80	/	[60]
ITO/PET/$MAPbI_3$/ITO/ Al_2O_3	0.16	/	/	1.67×10^{-9}	1200	200	380(350-850)	[61]
ITO/$Cs_3Cu_2I_5$/ITO	0.0649	6.9×10^{11}	/	1.1×10^{-10}	26.2	49.9	265(200-400)	[62]
Stainless steel/Gd-dopedZnO/$MAPbI_3$/ITO	28 0.22	1.2×10^{12} 9.3×10^{9}	/ /	1.75×10^{-6}	400 300	500 800	250-1357 White light IR	[63]
Glass/2D polystyrene template/ $MAPbI_3$/1D nanograting/Au	12.67	6.28×10^{13}	/	1.9×10^{-10}	21	67	White light	[64]
PET/P-SWCNTs/$CsPbBr_3$/Au	41	1.67×10^{12}	/	1.6×10^{-6}	25	21	520(300-800)	[65]
ITO/PEDOT:PSS/ $MAPbI_{3-x}Cl_x$ /PCBM/ BCP or PFN/Al	/	$\sim10^{14}$	100	1×10^{-7}	1.8×10^{-4}	1.6×10^{-4}	550(300-800)	[29]
ITO/PTAA/$MAPbI_3$/C_{60}/BCP/Cu	0.32	1.5×10^{13}	256	2×10^{-9}	/	3.1×10^{-3}	532(545-776)	[66]
ITO/NiO_x:PbI_2/$MAPbI_3$/ C_{60}/BCP/Ag	0.41	10^{13}	112	2×10^{-10}	/	1.68×10^{-4}	532(450-750)	[67]
FTO/TiO_2/$MAPbI_3$/Spiro-OMeTAD/Ag	0.55	10^{12}	120	/	4.6×10^{-4}	9.4×10^{-4}	650(400-750)	[68]
FTO/TiO_2/Al_2O_3/PCBM/$MAPbI_3$/Spiro-OMeTAD/Au	0.4	10^{12}	80	1×10^{-11}	10^{-3}	3×10^{-3}	600(400-780)	[69]
Glass/F-doped SnO_2/ TiO_2/$MAPbI_{3-x}Cl_x$/Spiro-OMeTAD/Au	620	/			200	200	400-800	[70]
FTO glass/ZnO hollow balls/$CsPbBr_3$/GaN/In	0.23	2.4×10^{13}	/	/	281	104	375(300-550)	[71]
ITO/SnO_2/$(FASnI_3)_{0.6}(MAPbI_3)_{0.4}$ /P3HT/Au	/	10^{11}	/	3×10^{-7}	32	19	810(300-1000)	[72]

Device structure	Responsivity (A W^{-1})	D^* (Jones)	LDR (dB)	Dark current (A)	Rise time (ms)	Fall time (ms)	Detect wavelength (nm)	Ref.
ITO/PTAA/$MAPBI_3$/F8IC:PTB7-Th/C_{60}/BCP/Cu	0.43	2.3×10^{11}	191	3.4×10^{-8}	0.032	0.02	870(300-1000)	[73]
ITO/PEIE-ZnO/$FAPbI_3$ /TFB/MoOx/Au	/	5.3×10^{12}	148	3×10^{-7}	6.8×10^{-6}	3.9×10^{-6}	450(350-800)	[74]
Si-NPA/$MAPbI_3$/ZnO	8.13×10^{-3}	9.74×10^{12}	/	2.18×10^{-10}	0.2533	0.2304	780(400-1050)	[75]
3-MPS treated Si/metal/MoO_3/PEDOT:PSS/$MASn_xPb_{1-x}I_3$/$PC_{61}BM$/metal/MoO_3	0.2	10^{11}	100	2.8×10^{-7}	9×10^{-5}	2.27×10^{-3}	940(300-1100)	[76]
Double-twisted $MAPbI_3$–TiO_2–carbon fiber and CuO–Cu_2O–Cu wire	0.5629	2.15×10^{13}	/	10^{-11}	<200	<200	800(350-1050)	[77]
Si/SiO_2/$(C_4H_9NH_3)_2PbBr_4$	2100	/	/	10^{-10}	/	/	470(460-510)	[11]
Si/SiO_2/Ti/Au/$MAPbI_3$/ ZnO hybrid	4	1.74×10^{9}	20.15	8.3×10^{-11}	<400	<400	380(400-800)	[27]
Si/SiO_2/Au/$CsPbBr_3$	34	7.5×10^{12}	28	/	0.6	0.9	442	[28]
Substrate/graphene/$MAPbI_3$/ Au	5.6×10^{8}	2.8×10^{16}	92	4×10^{-10}	$1.9\text{-}9.1\times10^{-2}$	0.417-0.48	300-800	[44]
PI/Ni gate electrode/Al_2O_3/PVP/Al_2O_3/Gr/$MAPbI_3$/Au	115	3.12×10^{12}	/	/	2500	5300	515(300-950)	[78]
n++Si/SiO_2/ $(C_6H_5C_2H_4NH_3)_2SnI_4$/ Au	1.9×10^{4}	/	/		450	/	447(350-636)	[79]
Si/SiO_2/Au/PCN-S-$MAPbCl_xI_{3-x}$	1.7	1.1×10^{11}	/	10^{-11}	6.1	2.1	460-620	[80]
Si/SiO_2/Au/$MAPbI_3$	58.5	/	/	/	/	/	635	[81]
Si/SiO_2/PbS-SCN/$MAPbI_3$/Au	255	4.9×10^{13}	60	1.84×10^{-8}	43	43	365(365-1550)	[82]
Si/SiO_2/Au/$MAPbI_3$	22	/	/	/	<20	<40	405(405-532)	[83]
Si/SiO_2/Au/CuSCN or NiO/$CsPbBr_3$	11	1.8×10^{11}	55	3×10^{-7}	2650	4000	365(300-500)	[84]
Si/SiO_2/$FA_{0.7}Cs_{0.3}Pb(I_{0.8}Br_{0.2})_3$/Au	5	3.62×10^{13}	120	3.6×10^{-12}	0.11	0.35	450(300-750)	[85]
Si/SiO_2/Au/$MAPbI_{3-x}Cl_x$/CYTOP	14.5	/	/	/	2×10^{-4}	7×10^{-4}	254,350-730	[86]
Si/SiO_2/2D $PdSe_2$/Cs-doped $FAPbI_3$/Au	0.313	2.72×10^{13}	/	/	3.5×10^{-3}	4×10^{-3}	800(200-1550)	[87]
Si/SiO_2/SU-8 photo-resist template/ $MAPb(I_{1-x}Br_x)_3$/Al/Ca	12500	1.73×10^{11}	150	/	3400	4200	650(370-780)	[88]
Si/SiO_2/$MAPbI_3$/Au/PbSe quantum dot	1.2	3.3×10^{7}	/	/	2.5	3	300(300-1500)	[89]
Nb:STO/PLZT/graphene/$MAPbI_3$/PCBM/Au	7×10^{6}	7×10^{12}	/	/	16000	68000	550(400-800)	[90]

*The red, yellow, green sections represent the metal-semiconductor-metal, photovoltaic, field-effect transistor-type detectors, respectively.

2.2. The structure and mechanism of photodetectors

The device architecture of a photodetector can mainly be classified into *vertical* and *lateral* structures, with the former being also called photovoltaic-type (or photodiode) and the latter being known as photoconductive-type, which in turn consists of the metal-semiconductor-metal (MSM) and the field-effect transistor (FET) configurations (**Figure 2a-b**). Among these three layouts, the MSM structure can be more straightforwardly fabricated and results in higher figures of merit (e.g., responsivity, EQE, gain) than the photovoltaic counterparts. However, photoconductive detectors suffer from a large dark current and long response time.[91] In contrast, photovoltaic-type detectors exhibit high response speed, large LDR, low noise, and minimal dark current. FET-type detectors, on the other hand, combine the characteristics of photovoltaic-type and MSM-type with balanced performances like low dark current and high responsivity.

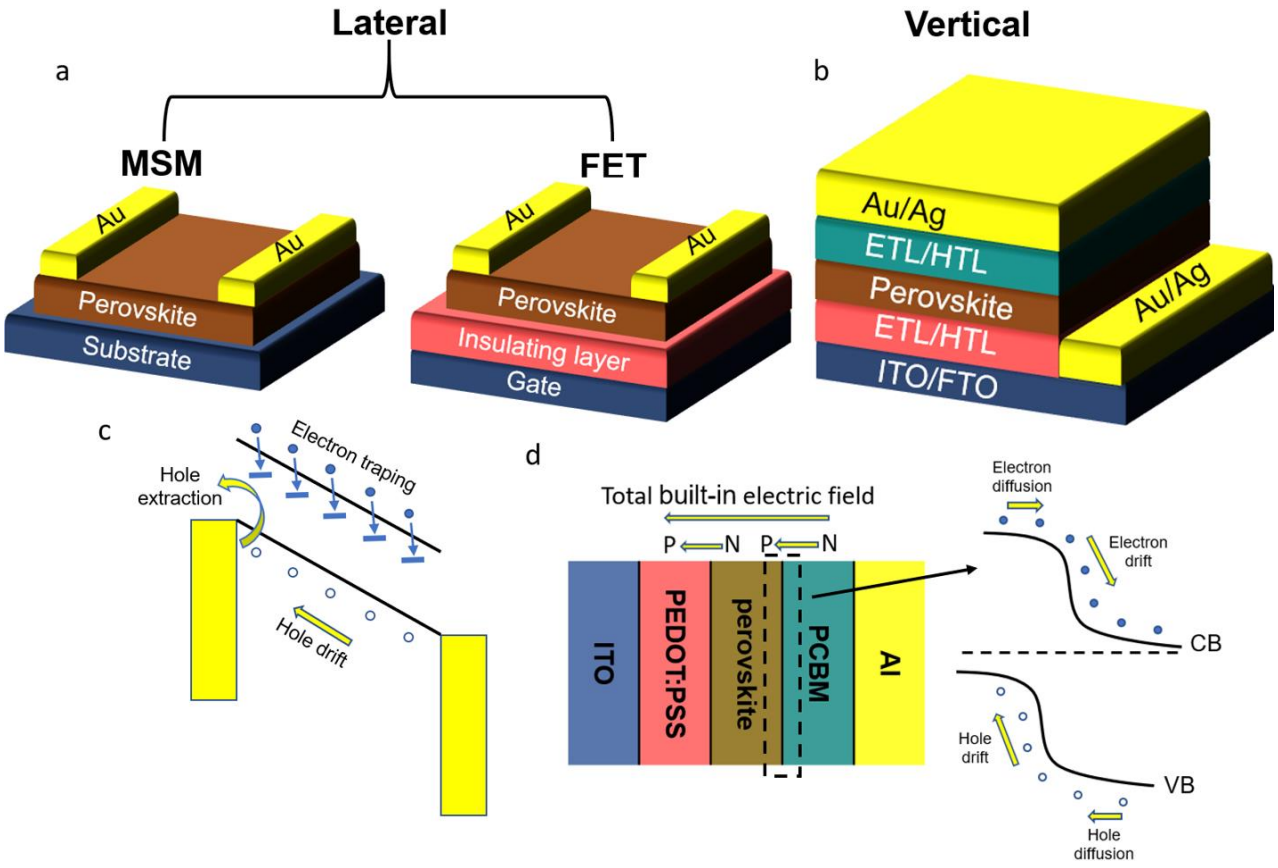

Figure 2. Typical device structures of (a) photoconductive-type photodetectors and (b) photovoltaic-type photodetectors. Charge-separation mechanisms of (c) photoconductive-type

photodetectors. The conduction band electrons are captured by associated trap states, and the holes drift under the influence of an electric field; (d) photovoltaic-type photodetectors. Drift and diffusion of both electrons and holes.

The differences in the intrinsic nature of the photodetectors based on MSM, PV, and FET structures can be visualized in **Figure 3**, in which the concrete data of typical key figures-of-merit are extracted from Table 1. For the $MAPbI_3$ perovskite, it is apparent that the PV-type detectors have a low response time of about 10^{-3} ms as well as low responsivity of about 0.4 A W^{-1}. In contrast, the MSM-type detector exhibits higher responsivity, together with a four orders of magnitude longer response time as compared to PV-type detectors. Although the responsivity of field-effect-type detectors is exceptionally high (5.6×10^{8}A W^{-1}), the response time is compromised. In this section, we will discuss the development of perovskite-based photodetectors in terms of the aforementioned three types of device structures.

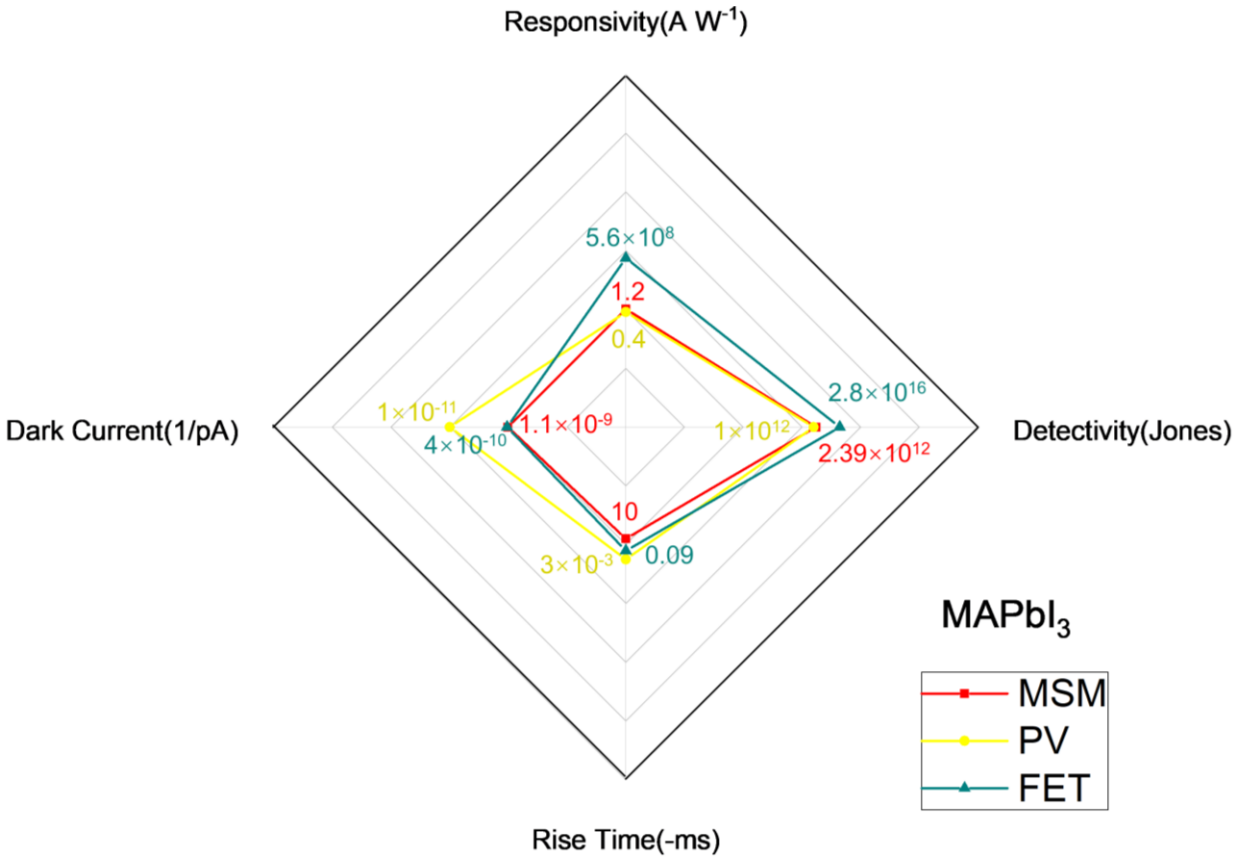

Figure 3. Key figures-of-merit of photodetectors based on MSM, PV, and FET structures.

2.2.1. Photoconductive-type detector

The photoconductive-type detectors operate on the concept of increasing electrical conductivity via the creation of free charge carriers within the semiconductor through light exposure. As shown in Figure 2c, if the lifetime of holes is long enough to pass through the device and external circuit many times, while the electrons stay trapped, a high photoconductive gain can be achieved.[92] The traps delay band-to-band recombination and impede the extraction of the trapped carriers. Therefore, EQE over 100% can be achieved, leading to high photocurrent and responsivity. However, due to large electrode spacing, photoconductive-type detectors usually show slow response and require high driving voltage.

Metal-semiconductor-metal structure

The metal-semiconductor-metal (MSM) structure is formed by depositing interdigital metal electrodes on both surfaces of the semiconductor layer, and the fabrication process is more straightforward than photovoltaic-type and FET-type detectors (*vide infra*). Hu et al. reported the first perovskite MSM photodetector using an ITO-$CH_3NH_3PbI_3$-ITO structure with a broadband response ranging from the ultraviolet to the entire visible spectrum. Photocurrents are generated though an externally applied potential in the opposite direction of the Schottky barrier and collected by the ITO electrodes. Under 3 V bias, the device showed photoresponsivity of 3.49 A W^{-1} and an EQE of 1.19×10^3 % at 365 nm. At 780 nm, the same parameters decreased to 0.0367 A W^{-1} and 5.84%, respectively.[93] Using inkjet printing of $CH_3NH_3PbI_3$ perovskites, Liu et al. fabricated MSM photodetectors with various morphologies by changing the solvents and by controlling the crystal growth rate (**Figure 4**).[57] Moreover, Zhou et al. compared the detective performances of three-layered two dimensional (2D) perovskite materials ($(C_4H_9NH_3)_2PbI_4$, $(C_4H_9NH_3)_2(CH_3NH_3)Pb_2I_7$ and

$(C_4H_9NH_3)_2(CH_3NH_3)_2Pb_3I_{10}$) in MSM type photodetectors. They found that $(C_4H_9NH_3)_2(CH_3NH_3)_2Pb_3I_{10}$ with the highest number of inorganic lead halide layers showed the best performance (responsivity of 12.78 mA W^{-1}, rise and fall time of 10.0 and 7.5 ms) due to the smallest bandgap and more condensed microstructure.[94]

It is interesting to see that the detector based on microwires showed low defect density and high coverage, resulting in a switching ratio of 16000%, a responsivity of 1.2 A W^{-1}, and a normalized detectivity of 2.39×10^{12} Jones at a light power density of 0.1 mW cm^{-2}. To increase the thermal stability, Zeng and his colleagues fabricated the first all-inorganic perovskite-based photodetector with $CsPbBr_3$ nanoplatelets as the responsive material. The device showed the largest responsivity of 34 A W^{-1} with a small bias of 1.5 V.[28] The high responsivity can also be ascribed to the unique morphology of the $CsPbBr_3$ nanoplatelet, which increased light absorption and in-plane charge carrier transport. For solar cell applications, the current typical perovskite films are polycrystalline, containing grain boundaries, pores, and surface defects. Single crystal perovskites, on the other hand, reduce those grain boundaries and the trap state density, thus significantly improving the electron and hole mobilities. This enables single-crystal perovskite with enhanced performance when used as photodetectors.[95,96] Via a template-assited method and a protective hydrophobic layer, Li et al. prepared a flexible photodetector based on $MAPbBr_3$ single-crystal microwire arrays, which developed a responsivity of 20 A W^{-1} and D* of 4.1×10^{11} Jones.[97] More importantly, the photodetector demonstrated significant stability. Without any encapsulation, the initial photocurrent was maintained at 96% over one year, without major losses in performance when kept in an enviroment of 60% RH for ten days.

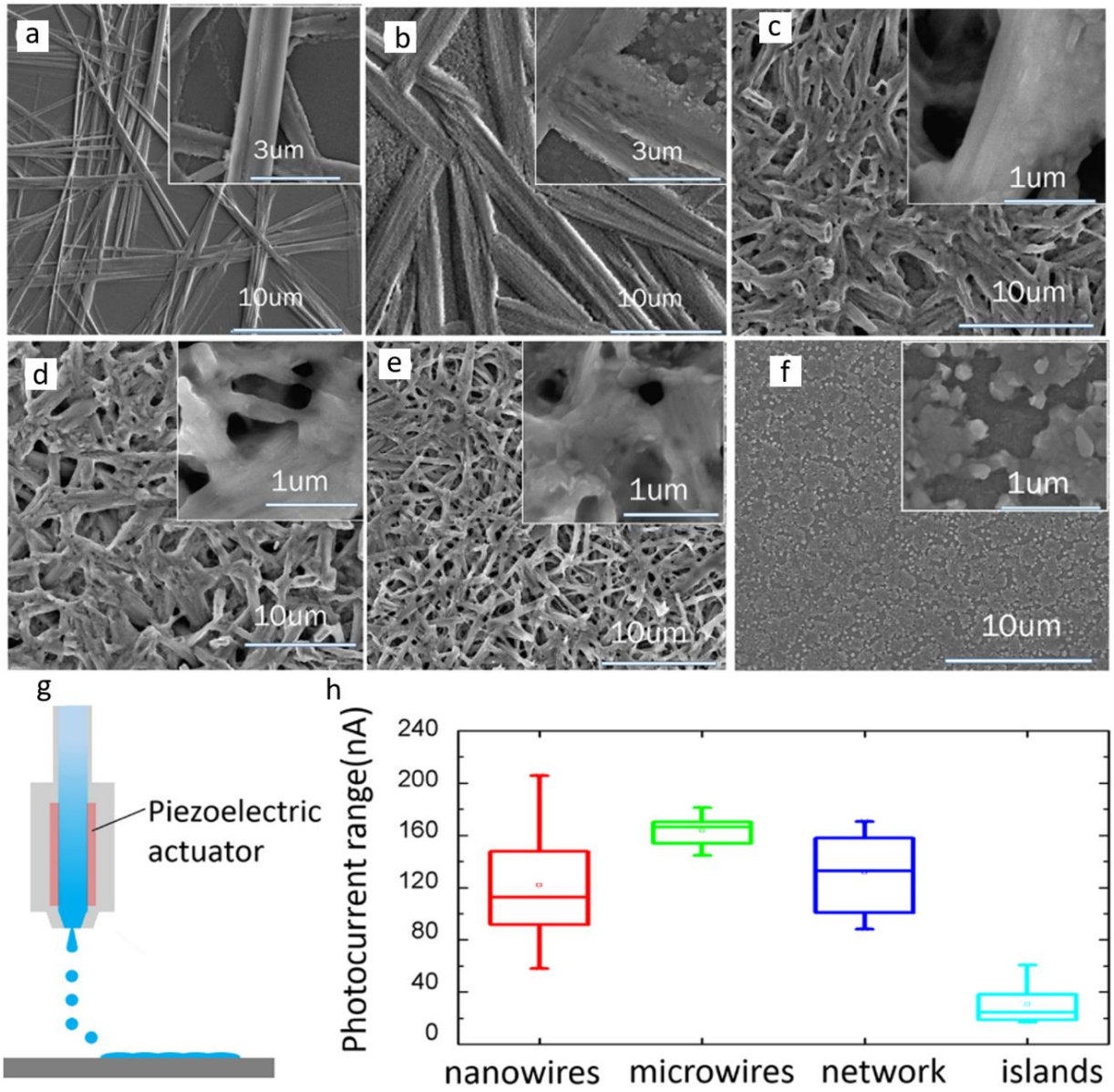

Figure 4. SEM images of different perovskite morphologies at a substrate temperature of (a) 25 °C, (b) 35 °C, (c) 45 °C, (d) 55 °C, (e) 65 °C, and (f) 75 °C, respectively. (g) Schematics of inkjet printing on ITO substrates. (h) Photocurrent statistical box plots of photodetectors based on nanowires, microwires, a network, and islands. Reproduced with permission.[57] Copyright 2015, American Chemical Society.

Field-effect transistor structure

A field-effect transistor (FET) is a voltage-controlled device that composes of a gate electrode, insulating gate layer, channel layer, and source/drain electrodes. The FET-type

detector features low dark current, high EQE, and high responsivity with reduced noise and amplified signal. Across the thin insulating layer between the gate and the semiconductor channel, the charge transfer characteristics in the semiconductor can be tuned by the applied gate voltage. When the device is operated at cumulative mode under forward bias gate voltage, a conductive channel of electrons (n-type) is produced between the source and the drain electrode. The accumulated electrons can be swept from source to drain under applied bias with a lower chance of recombination, therefore prolonging carrier lifetime, in this way yielding higher responsivity. In the dark, the concentration of carriers participating in the conduction is reduced, resulting in low dark current. Li et al. reported the first FET-type photodetector based on $CH_3NH_3PbI_{3-x}Cl_x$, obtaining a photoresponsivity of 320 A W^{-1}, which is among the most significant values reported for phototransistors at that time.[98] In contrast, Song et al. fabricated ultrathin $CH_3NH_3Pb(I_{3-x}Br_x)$ perovskite films with nearly single unit cell thickness (~1.3 nm) as the channel material in FET structured detectors (**Figure 5a-c**).[83] The detection range of the device ranges from UV to the visible spectrum. When the current gain was probed by lasers at wavelengths of 405 and 532 nm, the responsivities are merely 22 and 12 A W^{-1} at 1 V, respectively.

It is worth noting that the use of graphene in photodetectors become popular, especially for devices with FET architecture. Graphene is an attractive material with high charge carrier mobility and electrical conductivity, which, when combined with perovskite, leads to remarkable adsorption and responsivity as well as charge mobility in the so-called graphene FET (GFET) type photodetector.[25,99,100] Wang et al. demonstrated the first Ruddlesden–Popper-type layered perovskite $(C_4H_9NH_3)_2PbBr_4$ crystal-based photodetector with interdigital single-layer graphene as the electrodes and protective layer. They obtained both a high responsivity (~ 2100 A W^{-1}) and an extremely low dark current (~10^{-10} A).[11] Another example is the hybrid photodetector reported by Ahn et al., which showed a responsivity of 180 A W^{-1} and an effective quantum efficiency of 5×10^4 % at an illumination power of 1

μW (Figure 5d-f).[101] In this device, the valence band level of perovskite ($CH_3NH_3PbI_3$) is lower than graphene, facilitating electron transport from graphene to the adjacent perovskite layer to fill the empty states in the valence band caused by photoexcitation. This process can decrease the recombination rates of carriers. In contrast to the devices fabricated on a rigid Si substrate, Dang et al. published a flexible perovskite ($CH_3NH_3PbI_3$)-graphene FET on polyimide substrates, resulting in a high responsivity of 115 A W^{-1} at 515 nm as well as high durability after 3000 bending cycles at a 12 mm bending radius.[78] However, the response time of such kind of devices was limited by the low transfer rate due to the defect sites at the graphene/perovskite interface. To solve the problem, Qin et al. fabricated a bulk heterojunction film by mixing $CH_3NH_3PbI_3$ perovskite with [6,6]-phenyl-C_{61}-butyric acid methyl ester (PCBM) to enhance the charge carrier separation efficiency using PCBM as the electron acceptor.[102] This device yielded a photogating effect, with the photo-generated electron-hole pairs being separated in the presence of PCBM and transported to the graphene layer beneath the perovskite (Figure 5g-i). Thus, an extremely high photoresponsivity of $\approx 10^6$ A W^{-1} was achieved due to the high mobility of graphene, which was 30-fold higher than previous perovskite–graphene photodetectors. Furthermore, remarkable gate tunability was attained via shifting of graphene‘s Fermi energy with respect to the valence band maximum (VBM) and conduction band minimum (CBM) of the perovskite. A bulk heterojunction (BHJ) film was deposited on $Pb_{0.92}La_{0.08}Zr_{0.52}Ti_{0.48}O_3$ (PLZT) gated GFETs, resulting in a high-efficiency bipolar GFET with a small bottom-gate voltage (V_{bg}) of ~ ± 1 to 2 V. A photoresponsivity of 7×10^6 A W^{-1}, D* of 7×10^{12} Jones, and a corresponding photoconductive gain of 10^8 was acquired, which are almost 2 orders of magnitude higher than those of the BHJ/graphene device without gate tuning (Figure 5j-l).[90]

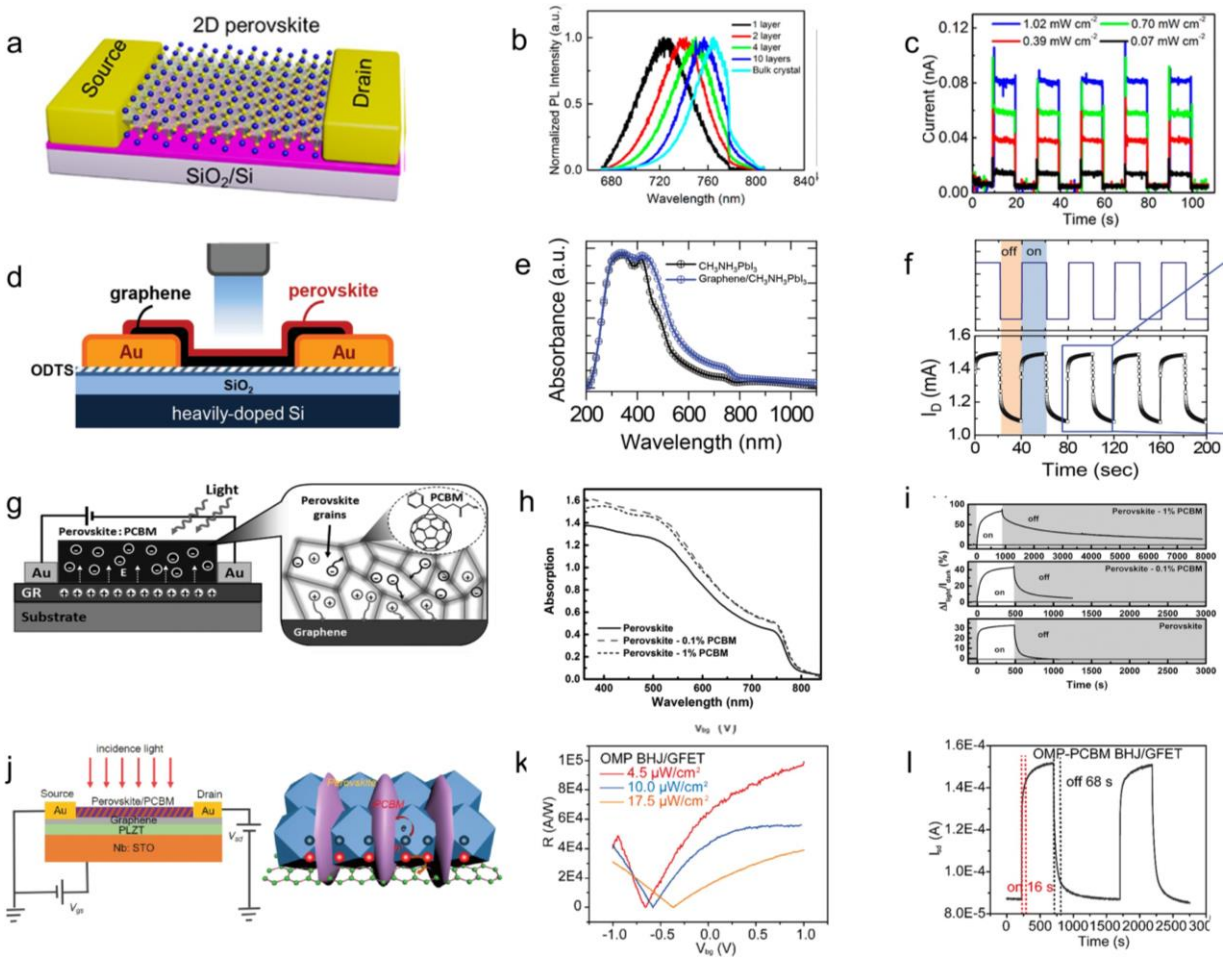

Figure 5. (a) Schematic image of a transistor device based on 2D perovskite. (b) Normalized PL spectra of 2D perovskite nanosheets with different thicknesses. (c) Time-dependent photocurrent measurement on the 2D perovskite phototransistor. Reproduced with permission.[83] Copyright 2017, American Chemical Society. (d) Schematic diagram of the device. (e) UV-VIS absorption spectra of the pristine $CH_3NH_3PbI_3$perovskite and $CH_3NH_3PbI_3$ perovskite-graphene hybrid films. (f) Photo-switching characteristics of the photodetector. Reproduced with permission.[101] Copyright 2015, Royal Society of Chemistry. (g) A schematic diagram of the BHJ/graphene photodetector. (h) UV-vis absorption spectra of the perovskite–PCBM BHJ films on graphene with different PCBM concentrations: 0%, 0.1%, and 1%. (i) The dynamic responses of devices with different PCBM concentrations. Reproduced with permission.[102] Copyright 2016, American Chemical Society. (j) Schematic illustration of the OMP-PCBM BHJ/GFET device. (k) Responsivity of the OMP-PCBM BHJ/GFET device versus V_{bg} under different light illuminations. (l) Dynamic responses of the OMP-PCBM BHJ/GFET device. Reproduced with permission.[90] Copyright 2018, American Chemical Society.

2.2.2. Photovoltaic-type device structure

Compared to photoconductive- and FET-type devices, the photovoltaic-type devices can operate at low or even no voltage bias and can work as self-powered devices. The light-sensitive materials absorb the incident photons to produce electron-hole pairs, which are then separated by the built-in electric field at the P-N junction. The photovoltaic effect is achieved via the accumulation of charge carriers on both sides of the depletion region. Due to the small electrode spacing resulting in short carrier transit length, photovoltaic-type devices normally show fast responses. In addition, the introduction of selective contact layers may help reduce the dark current/noise and increase detectivity/LDR. For example, when perovskite and PEDOT: PSS forms the P-N junction, the built-in electric field points to PEDOT: PSS at the interface, which is acting as the P-type layer. Meanwhile, at the P-N junction between perovskite and PCBM, the built-in electric field is directed towards the perovskite, acting as the P-type layer. Therefore, the total built-in electric field is in the direction from PCBM to PEDOT: PSS, resulting in two space-charge regions that prevent charge recombination. By applying an external potential bias in the same direction as the internal electric field, the space charge region of the two P-N junctions can be extended, resulting in both reduced carrier recombination and dark current. Upon illumination of the perovskite absorber, the holes move to the low-lying valence band of PEDOT: PSS and reach the ITO electrode, while the electrons migrate to the conduction band of PCBM and reach the Al electrode, forming a large photocurrent (Figure 2d).[29]

Utilizing perovskite materials with high EQE from 300 to 800 nm, Hong et al. reported a novel solution-processed $CH_3NH_3PbI_{3-x}Cl_x$ photodetector based on photovoltaic-type device with a structure of ITO glass/PEDOT:PSS (hole-transporting material, p-type layer)/$CH_3NH_3PbI_{3-x}Cl_x$/ PCBM (electron-transporting material, n-type layer)/BCP(2,9-dimethyl-4,7-diphenyl-1,10-phenanthroline) or PEN(poly[(9,9-bis(3’-(N,N-dimethylamino)propyl)-2,7-fluorene)-alt- 2,7-(9,9-dioctylfluoren)(acting as cathode contact

buffer/hole blocking layer to reduce charge recombination and dark current density)/Al electrode (**Figure 6a-c**).[29] The photodetector demonstrated a rectification ratio of ~ 10^5 (±1 V), high detectivities of 8 × 10^{13}, and 4 × 10^{14} Jones at -100 mV and 0 V, and a LDR of over 100 dB. Under different biases, there is minimal change in photocurrent, indicating undisturbed charge extraction. Liu et al. fabricated a photodetector device with an ITO/TiO_2/$PC_{61}BM$/$MAPbI_3$/P3HT/MoO_3 architecture in which the PCBM improves not only the transport performance but also passivates the sol-gel prepared TiO_2 film, resulting in reduced dark current densities (Figure 6d-f).[103] Zhu et al. substituted PEDOT: PSS with NiO_x in the nanocomposite with PbI_2 to function not only as an efficient hole extraction layer but also the seeds for the growth of the $MAPbI_3$ film. Owing to suppressed dark current, the device achieved a high responsivity in the visible spectral range of 450-750 nm and a fast fall time of 168 ns (Figure 6g-i).[67]

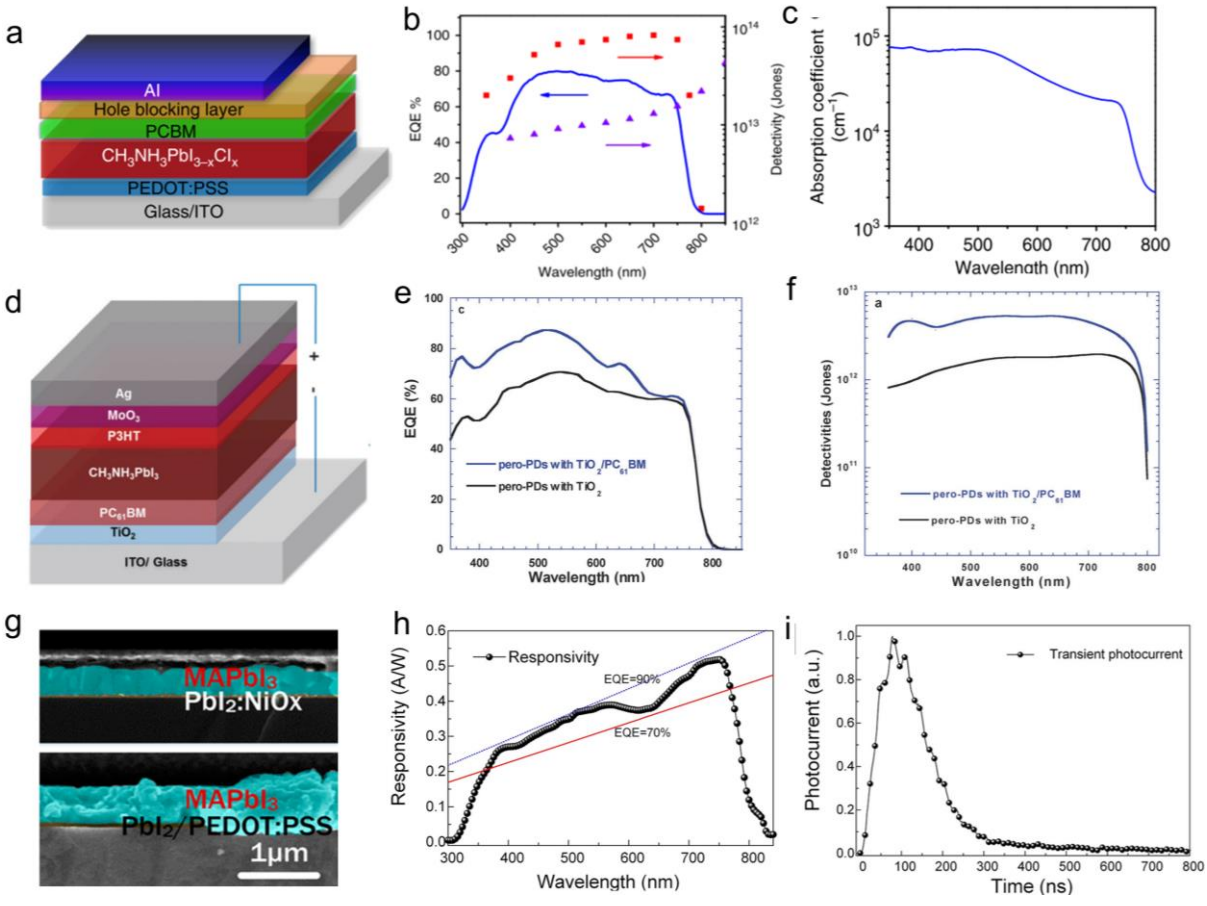

Figure 6. (a) Device structure of the hybrid perovskite photodetector; (b) External quantum efficiency and detectivity of the hybrid perovskite photodetector at different wavelength; (c) UV–visible absorption spectra of the photodetector without the hole-blocking layer and the Al electrode. Reproduced with permission.[29] Copyright 2014, Nature Publishing Group. (d) Device structure of hybrid perovskite photodetectors; (e) EQE spectra of hybrid perovskite photodetectors; (f) Detectivities versus wavelength of hybrid perovskite photodetectors. Reproduced with permission.[103] Copyright 2015, Royal Society of Chemistry. (g) Cross-sectional SEM images of the optimized NiO_x: PbI_2-based perovskite PDs; (h) Spectral responsivity as a function of response wavelength; (i) Transient photocurrent response of NiO_x: PbI_2-based perovskite PDs. Reproduced with permission.[67] Copyright 2016, American Chemical Society.

In 2015, Jinsong Huang's group reported a perovskite thin-film photodetector with an extremely low detection limit for visible light of sub 1 pW cm^{-2}, which was attributed to reduced noise signal via interface engineering and morphology improvement of the perovskite layer.[104] Nevertheless, the resistance-capacitance (RC) time constant limited the response speed. To solve this problem, they fabricated a high-speed perovskite photodetector with faster response time in the sub-nanosecond region by relieving the limit of the RC constant through the replacement of the $PC_{61}BM/C_{60}$ double electron extraction layer with C_{60}.[105] However, those devices mainly depend on polycrystalline films, which have a large number of grain boundaries that limit the performance. The same group further reported photodetectors based on perovskite single crystals in a vertical p-i-n structure, leading to low current noise of 1-2 fA $Hz^{-1/2}$ and high specific detectivity of 1.5×10^{13} Jones due to the absence of grain boundaries, in this way achieving lower charge recombination.[66]

2.2.3. Other types of device structures

In addition to the above-discussed typical device structures, there are other device architectures underlying the photovoltaic mechanism. For example, Sun et al. fabricated the first self-powered flexible fiber-shaped photodetector based on double-twisted perovskite-

TiO_2-carbon fiber and CuO-Cu_2O-Cu wire, as shown in **Figure 7a**.[77] Firstly, a thin layer of compact TiO_2 was coated on a highly flexible commercial carbon fiber, functioning both as electron transport and hole barrier layer. The fiber was then immersed into the perovskite solution to grow perovskite crystals. Subsequently, the CuO nanowire/Cu_2O compact film was deposited on a flexible Cu fiber as the electron barrier layer. Finally, the complete device was obtained by twisting the CuO-Cu_2O-Cu and the perovskite-coated fiber. In this device, TiO_2 prevented hole recombination on the anode. CuO transferred holes and broadened light response range to 1050 nm due to its narrow bandgap and suitable valence band level. Meanwhile, the higher conduction band of Cu_2O can hinder the back recombination of electron on the Cu cathode (Figure 7b). The obtained photodetector had a broadband responsivity in the range from ultraviolet (350 nm) to near-infrared (NIR) (1050 nm), detectivity of 2.15×10^{13} Jones, and responsivity of 562.9 mA W^{-1} at 800 nm. Additionally, a short response time of less than 200 ms was obtained, with no significant changes after dozens of cycles of bending to 90 degrees.

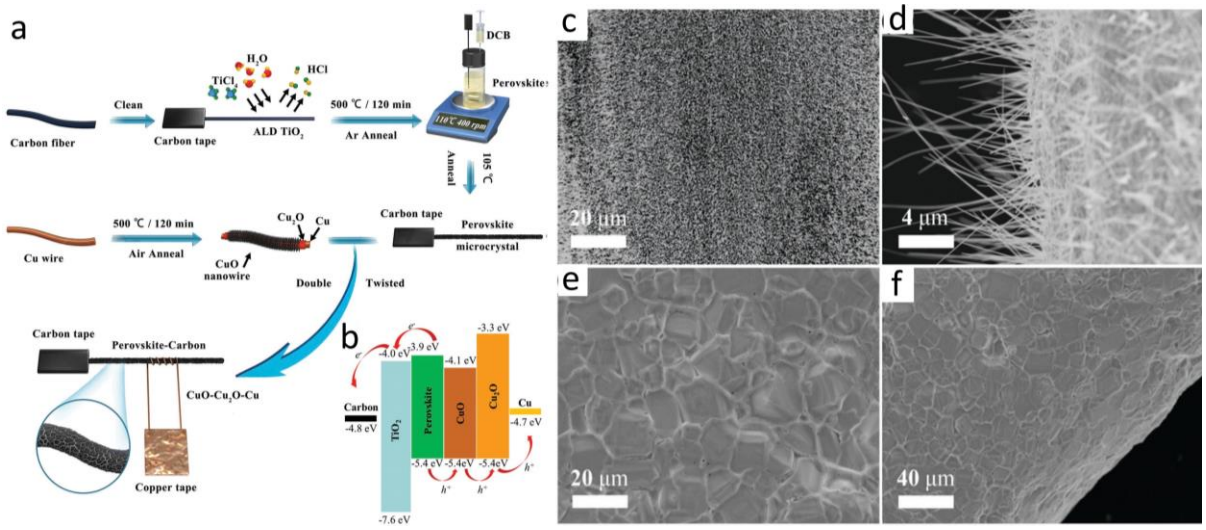

Figure 7. (a) Schematic illustration of the fabrication process of the fiber-shaped photodetector; (b) The energy-level diagram of photodetector device; (c) Top- and (d) side-view SEM images of annealed Cu wire; (e) Top- and (f) side-view SEM images of perovskite-coated carbon fiber. Reproduced with permission.[77] Copyright 2018, John Wiley and Son.

2.3. Broadband and narrowband photodetectors

Depending on the detection range, photodetectors can be classified into two main types. The first type involves broadband photodetectors capable of detecting electromagnetic waves from a wide range of wavelengths, such as from UV to IR or from visible to IR. The second type includes photodetectors for specified wavelengths (narrowband photodetector) sensitive to a narrow-range in the electromagnetic spectrum. **Figure 8** depicts the reported detection ranges of the same or different perovskite materials extracted from Table 1. Broadband photodetectors have applications in multicolor light detection and imaging. Depending on the bandgap of the perovskite materials, photodetectors usually show responses in the UV-vis region, which could be extended to the IR region by hybridizing with other inorganic or organic compounds or using mixed halide/Sn-Pb perovskites.[106–108] Narrowband photodiodes found applications in regular light-detecting, machine vision, and nano-optoelectronic integrated circuits, where differentiation of colors is usually needed. Conventionally, a broadband photodetector has to be used in combination with optical filters to narrow down the frequency of incoming photons.[109] However, the bandpass filter is expensive and complicated. Through the modulation of carrier collection efficiency, perovskite materials can achieve narrowband detection.[110,111]

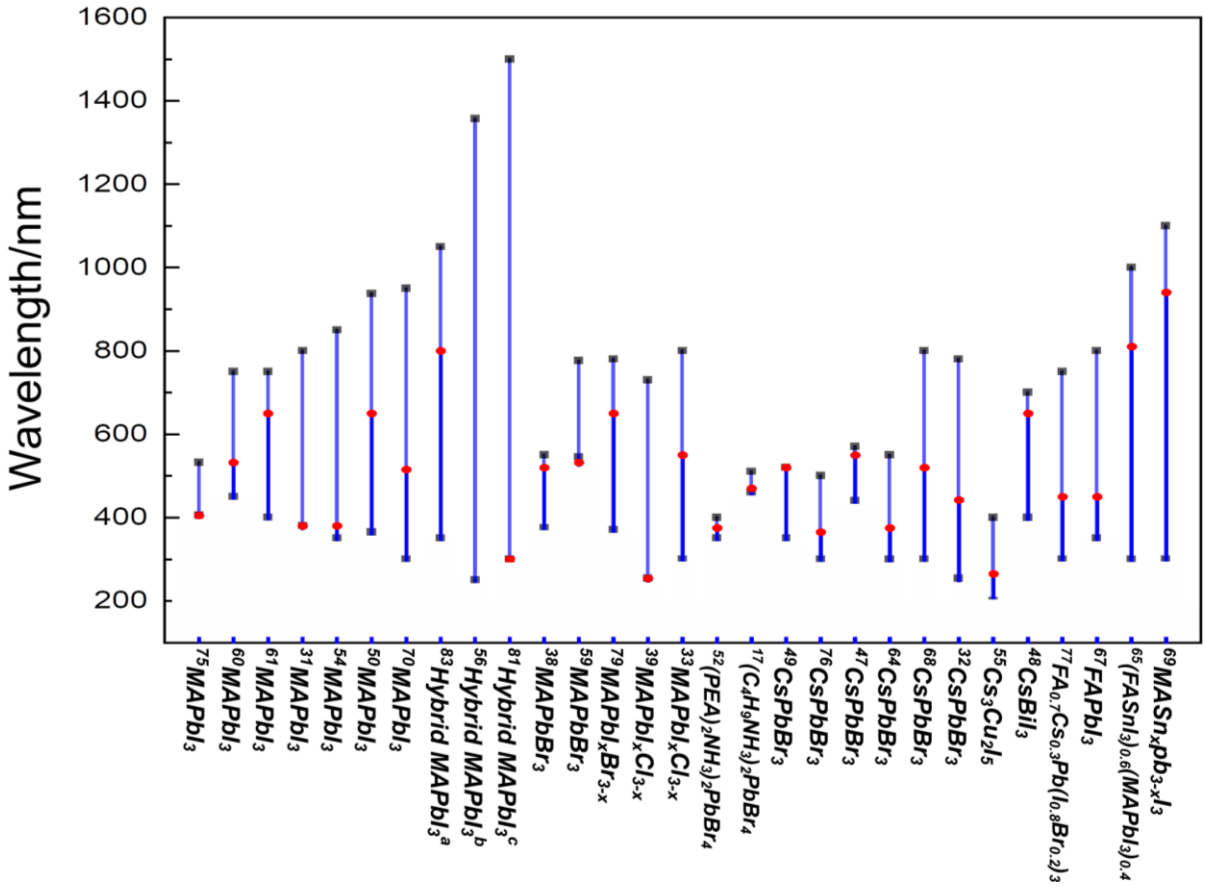

Figure 8. The wavelength detection range of different perovskite photodetectors. (The red dots represent the wavelength of light source for detectivity evaluation) ([a] Double-twisted $MAPbI_3$-TiO_2-carbon fiber and CuO-Cu_2O-Cu wire; [b] $MAPbI_3$/Gd-doped ZnO; [c] $MAPbI_3$/PbSe dots.)

For instance, $(PEA)_2PbBr_4$ is a wide-bandgap RP phase perovskite with a bandgap of 2.91 eV and strong absorption between 350 nm and 410 nm, rendering it an ideal material for UV detection. Therefore, Zhang et al. fabricated an array of photodetectors using a well-defined large-area (> 200 mm^2) single crystal of 2D $(PEA)_2PbBr_4$ via a controlled evaporation process (**Figure 9a-b**).[59] They obtained a low dark current of ~ 10^{-13} A, a large ON/OFF current ratio of ~ 10^5, a high specific detectivity of ~ 10^{13} Jones, and a fast response rate of ~ 0.4 ms at the detection wavelength of 365 nm. Since $MAPbBr_3$ has a bandgap of 2.24 eV, Saidaminov et al. fabricated large-area planar-integrated photodetectors for visible light (520 nm) detection using $MAPbBr_3$ single crystal with an ITO-semiconductor-ITO architecture.

Such devices yield a high gain of 10^4 electrons per photon and a high gain-bandwidth product of 10^8 Hz.[52]

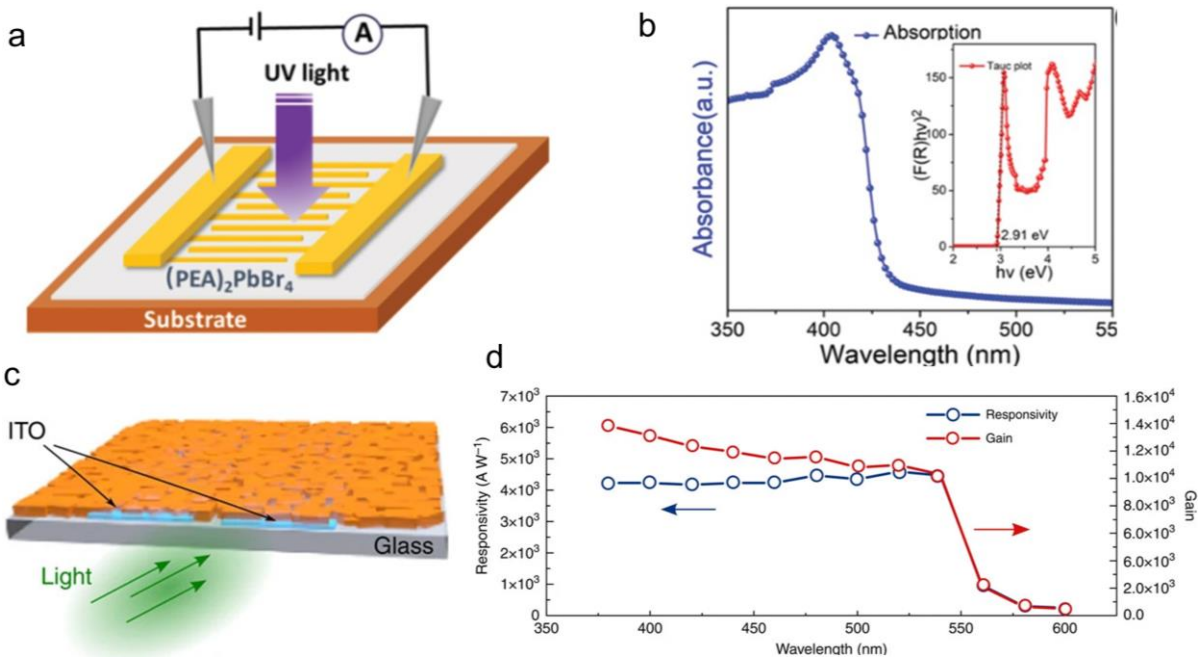

Figure 9. (a) Schematic diagram of the photodetector; (a) UV-Vis absorbance spectrum of the photodetector. Reproduced with permission.[59] Copyright 2019, Royal Society of Chemistry. (c) Three-dimensional illustration of the photodetector; (d) Responsivity and gain (external quantum efficiency) of the photodetector. Reproduced with permission.[52] Copyright 2015, Nature Publishing Group.

However, these narrowband perovskite photodetectors have several limitations. Firstly, their narrowband response originates from strong surface-charge recombination that quenches photo-generated charges by short-wavelength light. Moreover, the response time is long since thick perovskite crystals are normally used. As shown in **Figure 10a**, Li et al. defined an optically-active-but-electronically-dead (OAED) layer in the thick active perovskite film which only absorbs short-wavelength light but does not generate photocurrent due to the nonradiative recombination of photo-generated charges before they arrive at the electrodes. This phenomenon is caused by the active layer thickness exceeding the charge carrier diffusion length. To solve the problem, the authors proposed a novel method for tuning the response spectrum of the narrowband perovskite photodetector by using an extra wide-

bandgap perovskite $MAPbBr_{3-x}I_x$ as the external OAED layer.[112] The extra OAED layer was separated from the active layer by a glass electrode. The tandem photodetector consists of Cu/perovskite-1($MAPbBr_{3-x}I_x$)/TCO/perovskite-2($MAPbI_3$)/Cu. The detectable wavelength is controlled by the absorption edges of both the perovskite-1 and perovskite-2 layers. However, the response speed and response bandwidth are determined by the perovskite-2 layer since it has limited exposure to light. Finally, this narrowband photodetector demonstrated good color selectivity at 780 nm with an FWHM of 28 nm, a detectivity of 2.65×10^{12} Jones, an LDR of 190 dB, and a fast response speed up to the sub-nanosecond regime (> 10 MHz).

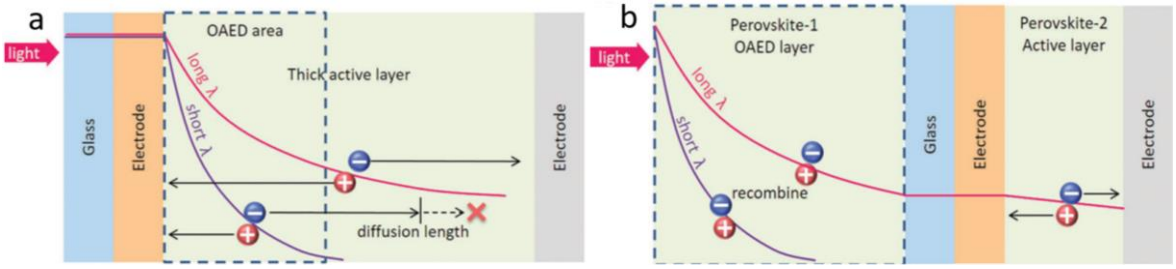

Figure 10. (a) Schematic of a narrowband photodetector containing a thick active layer. (b) Schematic of a narrowband photodetector with the new design. Reproduced with permission.[112] Copyright 2017, John Wiley and Son.

Furthermore, Wu et al. demonstrated FET type photodetectors that can distinguishably detect UV, visible and infrared spectra (**Figure 11**).[113] The active materials are hybrids of different perovskites with single-wall carbon nanotubes (SWCNTs). This integrated narrowband photodetector exhibited responsivity of 2×10^5 A W^{-1} to UV light at 365 nm at the region of $MAPbCl_3$/SWCNTs where no response to visible light was found. Meanwhile, the same device demonstrated a responsivity of up to 10^5 A W^{-1} at 365 nm and 10^3 A W^{-1} to visible light at 500 nm at the region of $MAPbBr_3$/SWCNTs. The authors also fabricated $MAPbI_3$/SCNTs hybrid devices for IR (800 nm) detection, of which, however, the data was not given. Serial devices containing both UV and visible photodetectors were constructed as well, resulting in different photocurrents for specific to UV, visible, and IR wavelengths.

More interestingly, Sun et al. fabricated a self-powered filterless color-sensitive photodetector based on tunable bandgap $KMAPbCl_xBr_{2-x}$ perovskite film with nanosecond response time.[114] Their innovation is that they deal the $KMAPbCl_xBr_{2-x}$ perovskite film between a hot heater (210 ℃) and a cold plate (-20 ℃). The temperature gradient enables control of the halogen ratios, in this way allowing bandgap tunability from 450 nm to 780 nm.

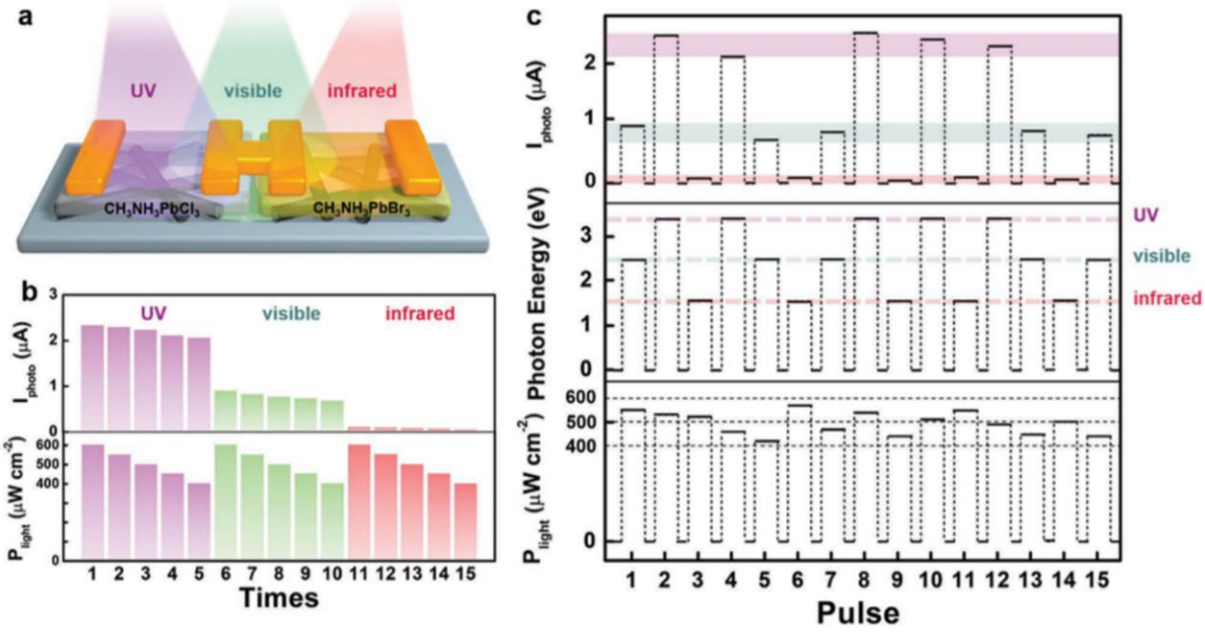

Figure 11. (a) Schematic configuration the serial $CH_3NH_3PbCl_3$/SWCNTs and $CH_3NH_3PbBr_3$/SWCNTs photosensors. (b) I_{photo} of the serial photosensors under illumination at different intensities in the UV, visible, and IR spectrum regions. c) Detection of the serial photosensors to randomly applied UV, visible light, and IR. Reproduced with permission.[113] Copyright 2018, John Wiley and Son.

Besides the effort towards high-performance narrowband perovskite photodetectors, to fabricate a single photodetector with a broader response range from UV to the IR region, it is necessary to use narrow bandgap perovskites or to combine the perovskite with other materials that have complementary light-absorbing abilities in IR or NIR range.[115–117] In this regard, Guo et al. demonstrated the first perovskite-based photodetector with responsivity covering from UV to visible light (350 nm to 730 nm) with 7.85 A W^{-1} for solar-blind UV light (λ = 254 nm) and 14.5 A W^{-1} to white light using $CH_3NH_3PbI_{3-x}Cl_x$ perovskite as the

absorbing material.[86] It is worthwhile to mention that they introduced a water-resistant fluorinated polymer (CYTOP) on the perovskite film as a protecting layer to increase the stability of the device (**Figure 12a-b**). To further extend the response of the perovskite device towards NIR photons, Yu et al. fabricated a broadband (300-1500 nm) photodetector based on a heterostructure of $CH_3NH_3PbI_3$ and PbSe colloidal quantum dot (Figure 12c-d).[89] The composite showed high and balanced carrier mobility (μ_n = 0.147 $cm^2\ V^{-1}\ s^{-1}$ and μ_p = 0.16 $cm^2\ V^{-1}\ s^{-1}$). Although the largest responsivity of merely 1.2 A W^{-1} was achieved at 460 nm, the fast response times (rise time of 2.5 ms and fall time of 3 ms) were impressive. In those previous works, near-infrared photodetectors based on perovskites were mostly fabricated by adding additional NIR absorbing layers. N. Alwadai et al. adopted an unconventional approach in which $MAPbI_3$ was deposited on metal-supported Gd-doped ZnO nanorods to achieve broadband (UV-IR, 250-1457nm) photodetection. A responsivity of 28 A W^{-1} and a detectivity of 1.1×10^{12} Jones for white light and 0.22 A W^{-1} and 9.3×10^9 Jones for IR light were achieved (Figure 12e-f).[63] The uniqueness of the device structure led to enhanced carrier injection and high responsivity, with the intraband transition in the perovskite material contributing to IR detection. They claimed the first pure perovskite-based photodetector with detection capability beyond 1000 nm. Due to the bolometric effect, Seebeck effect and pyroelectric effect, thermoelectric photodetectors have large response ranges up to the THz region. Combining photoconductive response in UV-vis range and bolometric response in MIR-THz range, $MAPbI_3$ photodetectors exported by Yao'group can achieve ultra-broadband with high responsity of 100 A W-1 in from 400-810 nm and 0.1 A W-1 from 110-1000 μm, respectively.[118] Their work provide novel insights into the thermoelectric characteristics of perovskite.

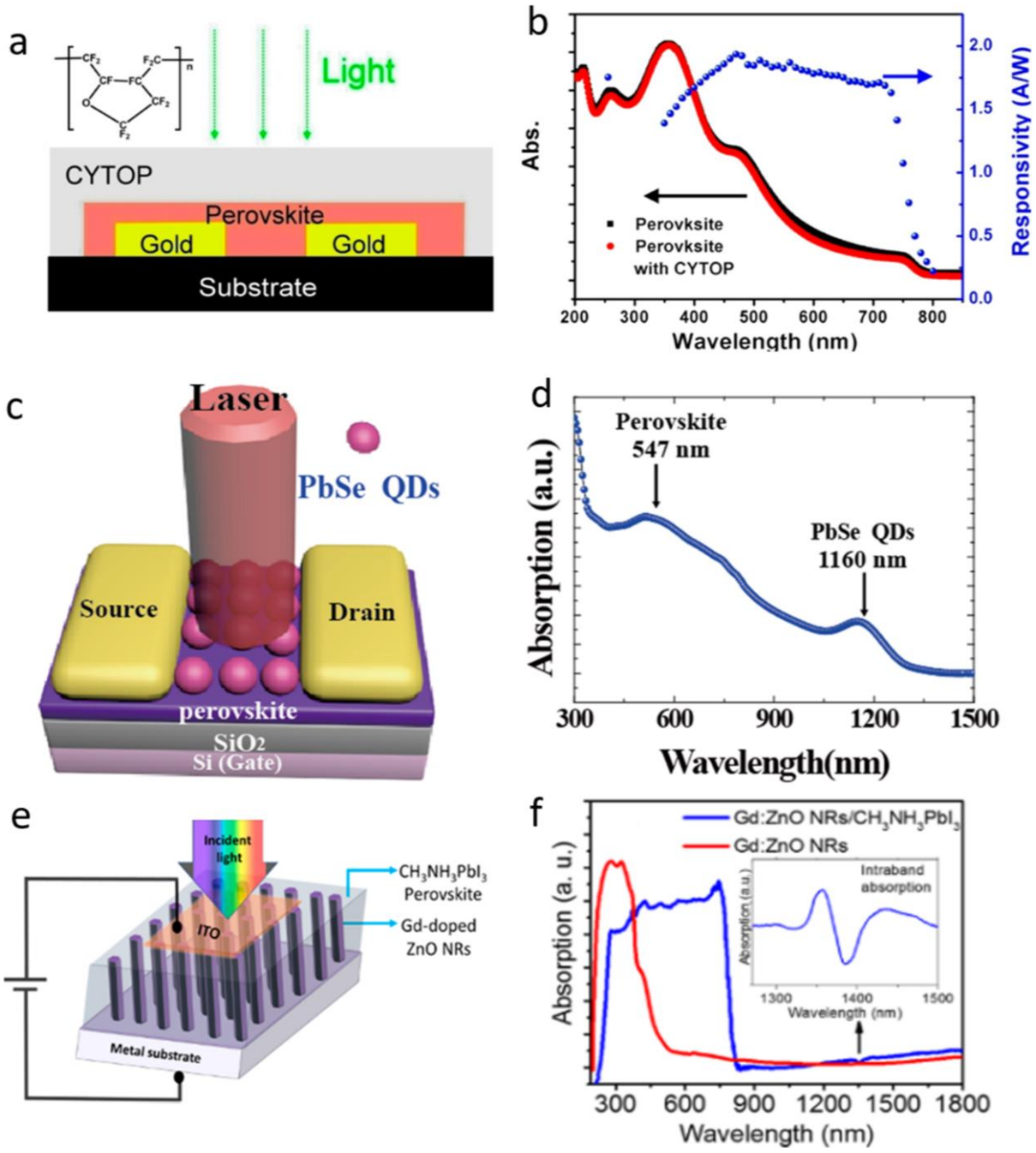

Figure 12. (a) CYTOP molecular structure and device configuration; (b) UV-vis absorption spectra of neat perovskite (black) and CYTOP-coated perovskite (red). Reproduced with permission [86] Copyright 2015, American Chemical Society. (c) Device schematic diagram; (d) The optical absorption spectrum of a hybrid including perovskite and PbSe QDs on a glass substrate. Reproduced with permission.[89] Copyright 2017, American Chemical Society. (e) Schematic diagram of photodetector architecture; (f) The absorption spectra of Gd-doped ZnO NRs and perovskite $CH_3NH_3PbI_3$. Reproduced with permission.[63] Copyright 2017, American Chemical Society.

2.4. Detector for high energy radiation

For high energy radiation detection and imaging, such as alpha particle, X-ray, and gamma-ray,[119–121] perovskite materials possess many advantages, such as broadly tunable bandgap of 1.6-3.0 eV, high-Z element Pb in the compound, and high charge carrier mobility/lifetime product ($\mu\tau$ ~10^{-2} cm^2 V^{-1}). The value of $\mu\tau$ determines the average carrier drift distance per unit electric field and hence the charge collection efficiency.[95,96,122,123] Researchers reported that $MAPbI_3$ could produce current when exposed to X-ray and could be used for bioimaging applications.[123] Furthermore, $MAPbI_3$ was shown to generate measurable current when exposed to ^{137}Cs gamma-ray.[96] As compared to the visible-light photodetector, detection of high energy radiation requires a much thicker active layer due to the amplified penetration capability of high energy photons such that charges can be generated across the entire thickness of the active layer.

In 2016, Wei et al. reported the first perovskite-based X-ray detector based on a $MAPbBr_3$ single crystal.[122] Due to the reduced bulk defects and passivated surface traps, a record-high $\mu\tau$ product of 1.8 × 10^{-2} cm^2 V^{-1} was achieved. In addition, the device reached a charge collection efficiency of 16.4% at a minimum X-ray dose rate of 0.5 $\mu Gy_{air}s^{-1}$ and sensitivity of $80\mu C\ Gy_{air}^{-1}cm^{-2}$. Later, they further studied the gamma-ray collection based on an alloyed perovskite of $CH_3NH_3PbBr_{2.94}Cl_{0.06}$. They employed a dopant compensation method to reduce the noise and carrier concentration in the bulk crystal, while improving the carrier mobility, lifetime and hence the charge collection efficiency.[121] Furthermore, as shown in **Figure 13a**, the author proposed a guard ring electrode around the central cathode to reduce the surface/edge leakage current since the outer guard electrode can absorb the leaking current near the surface/edge, leading to a bulk resistivity of $3.6\times10^9\Omega cm$. In the end, a well-defined ^{137}Cs energy spectrum was obtained with the alloyed perovskite single crystal under a

small electric field of 1.8 V mm^{-1} at room temperature, which is comparable or better than a standard scintillator detector.

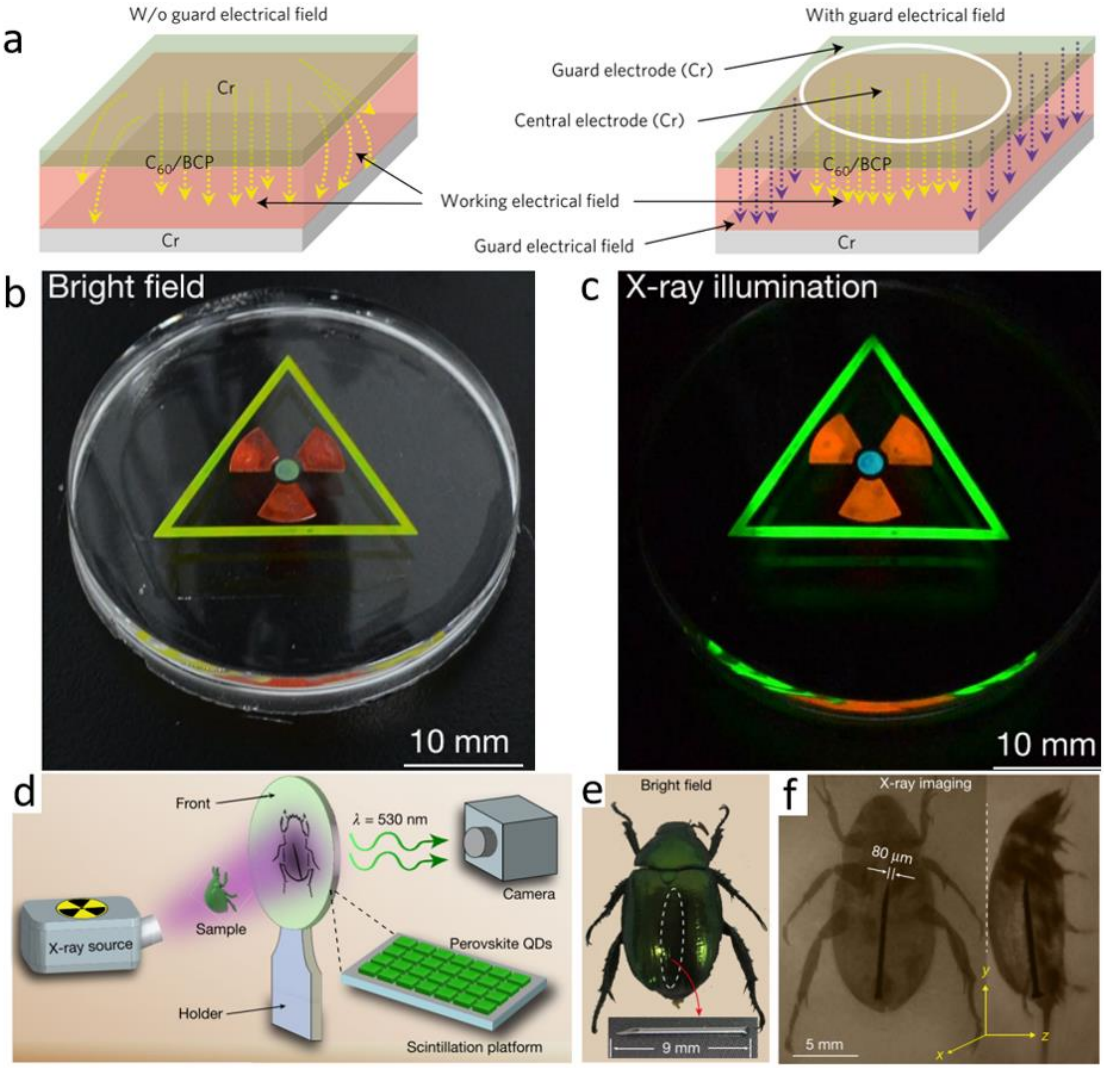

Figure 13. (a) Electric field distribution of a single-crystal device with a guard electrode. Reproduced with permission.[121] Copyright 2017, Nature Publishing Group. (b-c) Multicolour X-ray scintillation from three types of perovskite nanocrystal scintillator; (d) Schematic of the experimental setup; Bright-field (e) and the X-ray (f) images of the sample. Reproduced with permission.[124] Copyright 2018, Nature Publishing Group.

As a meaningful study, Tisadale et al. investigated the influence of precursor purity on the radiation sensing efficiency of solution-processed $MAPbBr_3$ single crystals.[125] As expected, they found that high purity precursors can lead to a factor of two to five larger single crystals on average compared to low purity precursors. Moreover, when subjected to

alpha radiation, the charge collection efficiency increased by 32±30% for high purity precursors. They proposed that impurities in the solution could affect the nucleation process, potentially suppressing the growth and arrangement of larger grains, ultimately leading to a large number of small crystals.

On the other hand, Wei et al. designed a simple technique to monolithically integrate $MAPbBr_3$ single crystals onto Si substrates with a structure of Si/$MAPbBr_3$/C_{60}/ BCP/Au.[126] A layer of (3-ammoniumpropyl)triethoxysilane bromide was used to mechanically and electrically connect the $MAPbBr_3$ single crystals with Si. From the electric signal directly read from Si, the device showed a low X-ray (8 keV) dose rate of <0.1 $\mu Gy_{air}s^{-1}$ with a sensitivity of $2.1\times10^4\ \mu C\ Gy_{air}^{-1}cm^{-2}$ for imaging capability. More importantly, the dose rate used here is 15 to 120-fold less than state-of-the-art technology, allowing lower X-ray exposure to patients. To further reduce the dose rate, Chen et al. introduced a flexible and highly sensitive X-ray detector using $CsPbBr_3$ quantum dots, exhibiting an extremely low dose rate of 13 nGy s^{-1}, about 400 times lower than typical medical imaging doses (Figure 13b-f).[124] Furthermore, the device is capable of emitting light in the visible range, thus permitting imaging by modulating the composition of perovskite quantum dots. This research could potentially provide a convenient visualization tool for real time, low-dose X-ray radiography. Zhang et al. grew ordered 3D $MAPbI_3$ nanowires arrays via a vapor-solid-solid reaction process and then applied it to a flexible imaging sensor (**Figure 14**).[127] Owing to the small nanowire diameter and high density of growth, the image sensor is composed of 1024 photodiode pixels over an area of 1.6384 cm^2 containing vertically grown $MAPbI_3$ nanowires.

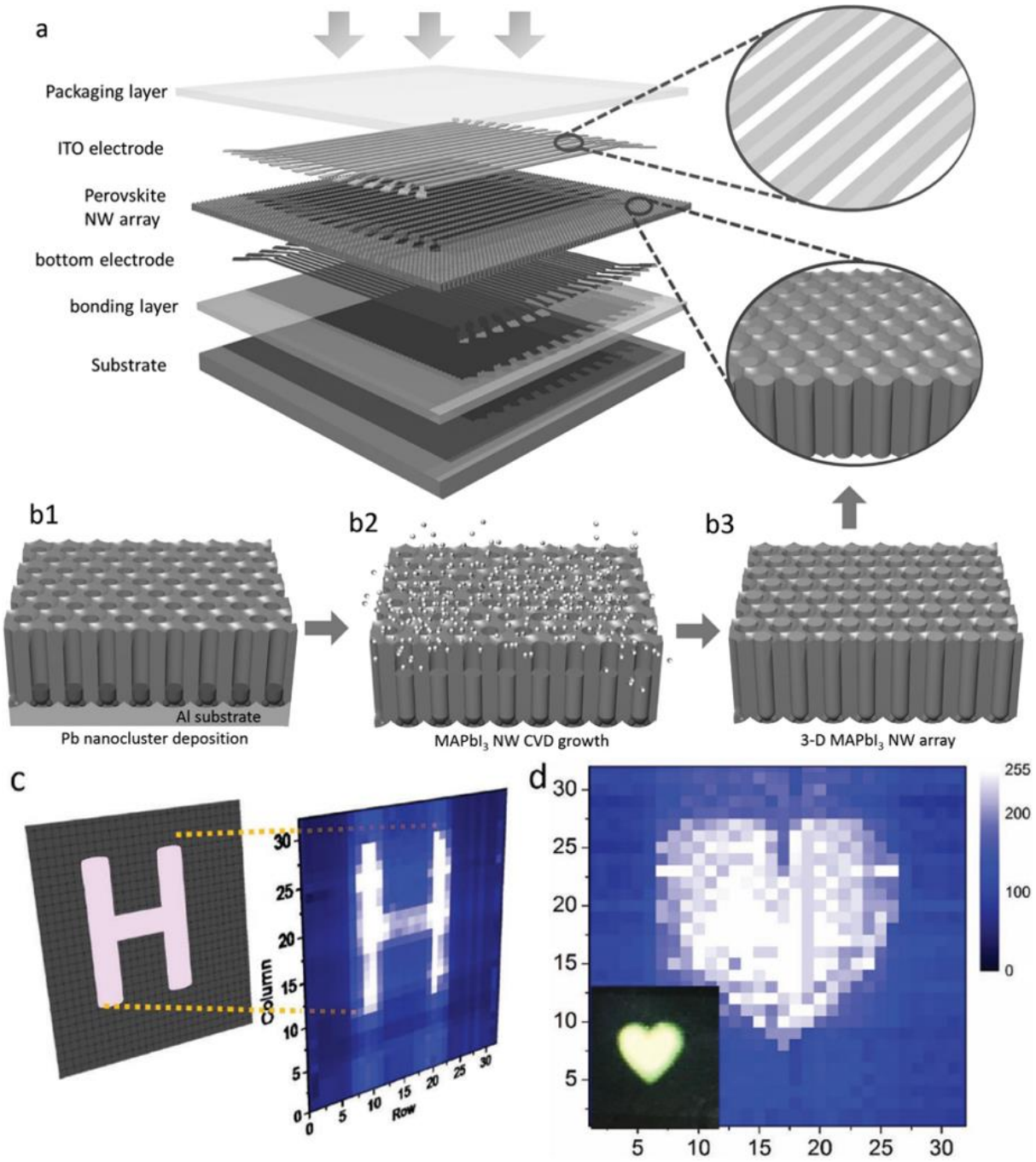

Figure 14. (a) Layer-by-layer structure of 32 × 32 $MAPbI_3$ NW image sensor; (b) Schematic of PAM template-assisted growth of $MAPbI_3$ NW array: (b1) Pb in PAM before NW growth;(b2) Partial $MAPbI_3$ NW growth in freestanding PAM; (b3) Completed $MAPbI_3$ NW growth in PAM; (c) Original and imaged letter ('H'); (d) Original and imaged love heart pattern. Reproduced with permission.[127] Copyright 2016, John Wiley and Son.

3. Other sensing or detecting applications

In general, 'sensor' is a broader concept than 'detector'. The definition of a sensor is a device that can convert the nonperceptable chemical or physical signals to quantificational data or non-quantitative signals. Sometimes, the sensing performance can be simply identified via changes in color. As for detectors, they usually denote a group of devices that apperceive electromagnetic radiations like visible light, X-ray and gamma-ray, etc. with different wavelengths or energies. They can convert the photon energy into electrical signals and determine its intensity and energy by the amplitude and magnitude. Another branch of the sensor family is Radar. Radar detects radio or microwaves which has much longer wavelengths to determine the range, angle, or velocity of objects. In terms of perovskite materials, it has been mainly considered for the application in the detection of high energy electromagnetic waves (from gamma-rays to near-infrared domains), as we have discussed in the above sections. In this new section, we will summary the application of perovskite materials in other sensing scenes, such as volatile organic compounds,[128] liquid/solid compounds,[129] pH value, and temperature,[130] and pressure.[131] (**Table 2**)

Table 2. Other sensor applications of perovskites

	Material	Substance	Performance	Ref.
Gas Sensor	$CH_3NH_3X_3$	ammonia	PL quenched by 60% to ammonia vapor from a 0.3 wt% ammonia solution	[30]
	$CH_3NH_3I_3$	pyridine	100 times reversible visible color change with fluorescence switching, ultra-fast (<1 s)	[128]
	$CH_3NH_3Br_3$	aliphatic amine	fast (<1 s), highly discernible (89%)	[132]
	$CsPbBr_3$ nanocrystals	HCl	5 ppm	[133]
	$CH_3NH_3PbBr_3$ nanoplates and nanowires	organic amines vapors	Fluorescence attenuation rate exceeded 90% for <4 s, color changed from yellow to white upon exposure	[134]
	$CH_3NH_3PbI_{3-x}(SCN)_x$	acetone NO_2	Sensitivities of 5.6×10^{-3}, the limit of 20 ppm Sensitivities of 5.3×10^{-1}, the limit of 200 ppb	[135]
	$(C_4H_9NH_3)_2PbI_4$	p-xylene	1 ppm with a response of 11.8 and response time at 140 °C and recovery time are 4.6s and 5.9s	[136]
	$CH_3NH_3Br_3$quantum dots@silica aerogels	SO_2	Linear relationship between the fluorescence intensity and concentration in the range of 0−10 ppm (> 3 Month)	[137]
	$CH_3NH_3PbI_{3-x}Cl_x$	ozone	70 s at 13 ppb, detection range from 2500 to 5 ppb	[138]
	Mn^{II}-doped $CsPbCl_3$	O_2	PL quenched by 53% on increasing O_2 concentration from 0 to 100%, linear relationship in 0-12%	[139]
	$CH_3NH_3SnI_3$	NO_2	Rg/Ra = 240 for 5 ppm, recovery within 12 s, detection limit (55 ppb), linear response between 0.5 and 10 ppm	[140]
Compound Sensor	$CH_3NH_3Br_3$	humidity	PL at 530 nm linearly quenched by a humidity increase from 7 to 98%.	[129]
	$CsPbBr_3$ quantum dots/polystyrene fiber membrane	Rhodamine 6G	Quantum yields (91%), 0.01ppm, nearly 100% fluorescence retention for 10 days in water	[141]
	$CsPbCl_3$ quantum dots modified TiO_2 inverse opal photonic crystals	Alpha fetoprotein	Linear range from 0.08 ng ml^{-1} to 980 ng ml^{-1}, detection limit is 30 pg ml^{-1}	[142]
	$MAPbBr_3$ in PVDF matrix	nitroaromatics, nitroamines, nitrate esters	Sensitive to few nanograms	[143]
	$CH_3NH_3PbI_{3-x}Cl_x$	humidity	Resistance drop from 1.28×10^8 at 30% RH to 7.39×10^4 at 90% RH	[144]
	$Cs_2BiAgBr_6$	humidity	Response/recovery time of 1.78/0.45 s at RH from 5% to 75%	[145]
Other Performance	$(C_nH_{2n+1}NH_3)_2PbI_4$	Temperature; Ph value	High sensitivity (1.3% K^{-1}) and good reversibility (>500 cycles) in a range of 0–80 °C; PL remains unchanged from 11.0 to 9.2, but increase from 8.4 to 3.0	[130]
	$CsPbBr_3$	peroxide in edible oil	The color changed from green to yellow and finally to red as the peroxide number decrease	[146]
	Mn-doped $CsPb(Cl/Br)_3$ quantum dots	temperature	PL intensity linearly change with T correlation coefficient up to 0.995	[147]

3.1. Gas sensors

So far, perovskite-based gas sensors operate on alterations in chemiresistivity or colorimetry. For instance, Kakavelakis et al. fabricated a self-powered ozone sensor working at room temperature based on $CH_3NH_3PbI_{3-x}Cl_x$ perovskite.[138] When exposed to ozone, the gas molecules diffuse within the perovskite lattice surface and passivate the traps, namely unpaired Pb^{2+} ions, thus resulting in the reduction of resistivity of the material. More specifically, the transfer of charges from ozone molecules to Pb^{2+} cation neutralize the excess positive charge and thereby adjuste the surface recombination rate. The device displayed an ultralow limit for ozone concentration detection, ranging from 2500 down to 5 ppb **(Figure 15a)**. However, the perovskite film would degrade gradually after 60 min. To improve stability, Zhuang et al. demonstrated a gas sensor based on thiocyanate ion-doped perovskite ($MAPbI_{3-x}(SCN)_x$) that could detect acetone vapor and NO_2 selectively with the limits of detection of 5.6×10^{-3} and 5.3×10^{-1} ppm^{-1}, respectively (Figure 15b-c).[135] The guest molecules capture the charge carriers when in contact with the perovskite film, resulting in an increase of resistance. This effect was reversible, with the device being stable for one week under a humidity condition of 30-60%.

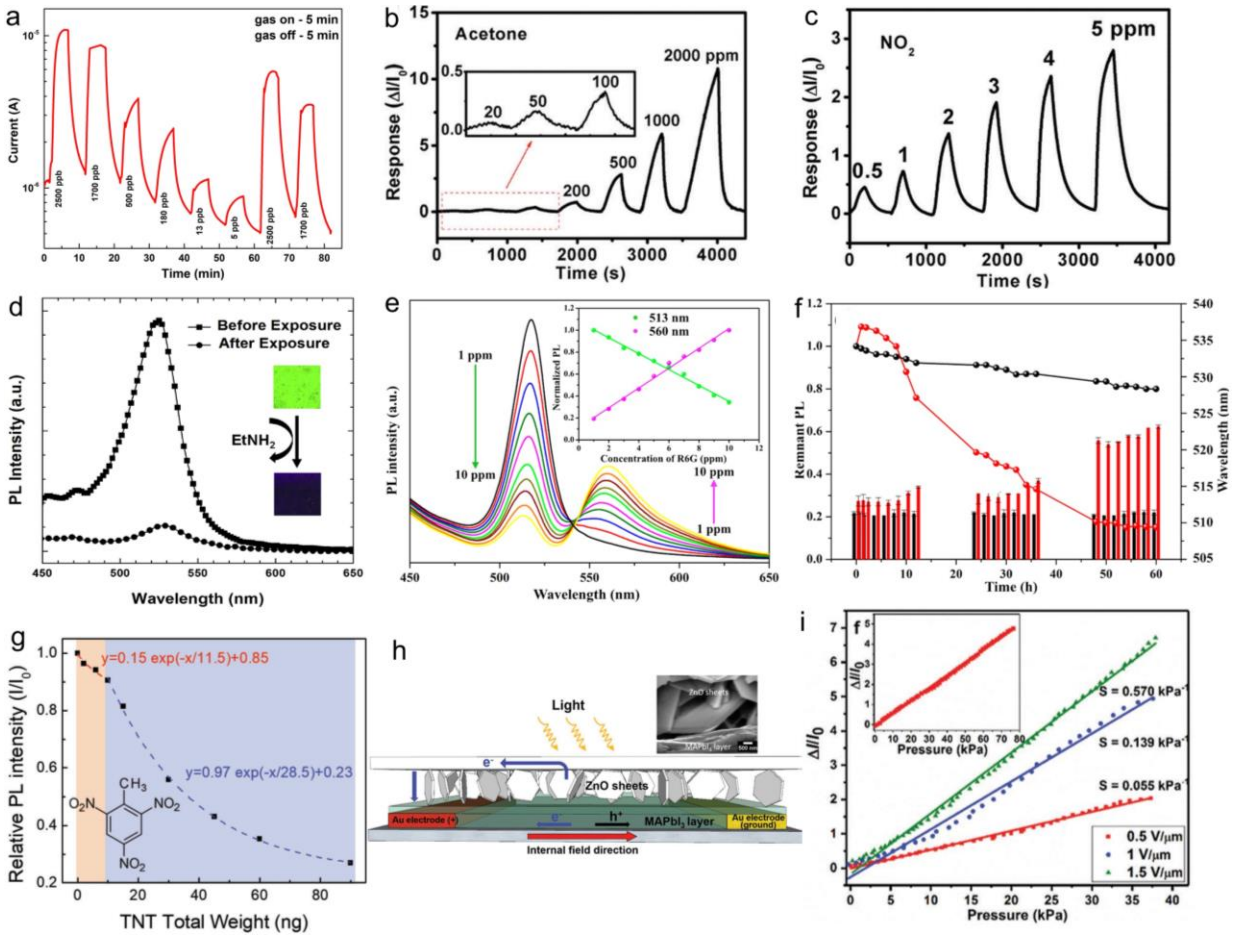

Figure 15. (a) The electrical response of the sensor based on $CH_3NH_3PbI_{3-x}Cl_x$ under various ozone concentrations. Reproduced with permission.[138] Copyright 2018, American Chemical Society. Plot of response versus time when exposed to (b) acetone vapours with concentrations ranging from 20 to 2000 ppm; (c) NO_2 at concentrations ranging from 500 ppb to 5 ppm. Reproduced with permission.[135] Copyright 2017, Royal Society of Chemistry. (d) PL intensity change of $CH_3NH_3PbBr_3$ film upon <1 s exposure to the monoethylamine vapor. Reproduced with permission.[132] Copyright 2017, Elsevier Ltd. (e) The PL spectra of CPBQDs/PS FM in R6G aqueous solution with concentrations from 1 to 10 ppm; (f) PL retention of CPBQDs/PS FM (black line with dots) and CPBQDs toluene solution (red line with dots), peak positions of CPBQDs/PS FM (black bars) and CPBQDs toluene solution (red bars) under 365 nm light. Reproduced with permission.[148] Copyright 2016, American Chemical Society. (g) The relative PL peak intensity with increasing TNT total weight. Reproduced with permission.[143] Copyright 2018, John Wiley and Son. (h) Schematic of the

solar-powered tactile sensor; (i) The sensitivity of the device versus pressure under different strength of the poling electric fields. Reproduced with permission.[131] Copyright 2018, John Wiley and Son.

The sensing of gas (or vapor) can also be indicated by the change of color and/or quenching of fluorescence, which could be observed by a spectrometer, machine vision system, or even naked eye. Kim et al. found that the color of $MAPbI_3$ perovskite film changed from dark brown to colorless within 1 second when exposed to pyridine vapor due to the formation of the hydrogen bonds between the perovskite and polar molecules.[128] This process is reversible and can be repeat more than 100 times. Furthermore, the same group reported the detection of aliphatic amine via reversible/irreversible fluorescence quenching of $MAPbBr_3$ perovskite nanoparticles through the same mechanism (Figure 15d).[132] The fluorescence quenching response of up to 89% was highly discernible within one second. The study suggested an effective strategy for naked eye-based fluorescence sensing of the colorless and harmful aliphatic amine vapors. Similarly, Ruan et al. reported an optical fiber-based sensor for ammonia gas using $MAPbX_3$ (X=Cl, Br, or I) as the indicator according to their recoverable PL quenching.[30] The phenomenon is due to reversible coordination of NH_3 molecules to $[PbI_6]^{4-}$ octahedral layer and the formation of $NH_4PbX_3 \cdot$ MA complex. Besides applications in sensing basic chemicals, perovskite-based sensors can also be used to detect acidic gases. Chen et al. utilized $CsPbBr_3$ nanocrystals as highly selective and sensitive spectrochemical probes for HCl gas with a limit of detection as low as 5 ppm.[133] They proposed an anion exchange between $CsPbBr_3$ and HCl as the underlying mechanism, resulting in a significant blue-shift in the ultraviolet-visible light absorption and PL spectra. During the anion exchange, the $CsPb(Br/Cl)_3$ nanocrystals retained the morphology and crystal structure of the initial $CsPbBr_3$ nanocrystals.

3.2. Chemical sensors in aqueous systems

The strategy of embedding perovskites in a polymer matrix was adopted by encapsulating $CsPbBr_3$ perovskite quantum dots into a monolithic superhydrophobic polystyrene fiber membrane by one-step electrospinning.[148] The obtained composites, called CPBQDs/PS FM, showed high quantum yields of ~91%, narrow half-peak width of ~16 nm, nearly 100% fluorescence retention after being exposed to water for 10 days, and 79.80% fluorescence retention after 365 nm UV-light illumination for 60 h (Figure 15e-f). Wang et al. used the composites to detect Rhodamine 6G in aqueous solution, displaying an ultralow detection limit of 0.01 ppm. The high durability, good tolerability, and recyclability of CPBQDs/PS FM renders it a potential candidate for practical applications. One year later, the same group replaced PS by polymethyl methacrylate (PMMA) to fabricate CPBQDs/PMMA FM using the same method. The authors found that the new perovskite-polymer composite can detect various compounds via a different mechanism. For example, it is a supersensitive sensor for trypsin with an extremely low detection limit of 0.1 $\mu g\ mL^{-1}$ via the cleavage of peptide CF6 (Cys-Pro-Arg-Gly-R6G). At the same time, owing to the high-efficiency fluorescence resonance energy transfer (FRET) process between the composite and cyclam-Cu^{2+}, an unprecedented detection limit of 10^{-15} M for Cu^{2+} was shown. Furthermore, the pH value can be confirmed by the composite in 10 ppb hydrazide R6G ethanol solution.[149] All these findings reveal outstanding sensitivity and stable detection performance of the CPBQD/PMMA FM.

The detection of explosive chemicals is critical for public security, where the perovskite-based sensors also be applied. Hao et al. embedded $MAPbBr_3$ nanocrystals in a poly(vinylidene fluoride) (PVDF) polymer matrix via the freeze-drying process, obtaining a porous nanocomposite that showed strong fluorescence quenching when exposed to various explosive compounds such as, 2,4,6-trinitrotoluene (TNT), 1,3,5-trinitroperhydro-1,3,5-triazine (RDX), and trinitroglycerin (TNG), with a high sensitivity of a few nanograms (Figure 15g).[143] The high porosity increased the specific surface area, thus enhancing the

absorption and diffusion process of explosive chemicals towards the perovskite nanocrystals. Meanwhile, the PVDF polymer matrix prevented the penetration of water and alcohol molecules into the composites due to the hydrophobicity. As a result, the nanocomposites exhibit excellent stability against moisture and solvents. The authors compared the performances of pristine perovskite film, dense PVDF-perovskite film, and porous PVDF-perovskite film, and found that the pristine perovskite film degraded instantly in the water, while PVDF-perovskite composite films were far more stable. However, the dense PVDF-perovskite film had negligible responses to explosives.

Targeting on heavy metal ions, Lu et al. proposed a fluorescence nanosensor using $MAPbBr_3$ perovskite quantum dots for detecting Hg^{2+} via surface ion-exchange, which could result in PL quenching.[150] Later, Liu et al. reported a fluorescent probe for selective detection of Cu^{2+} in hexane based on inorganic $CsPbBr_3$ perovskite quantum dots via electron transfer to Cu^{2+}.[151] Within seconds, the PL intensity of $CsPbBr_3$ PQDs was significantly quenched by Cu^{2+}, and the sensor showed a detection range from 0 to 100 nM with a limit of detection as low as 0.1 nM, indicating significant potential for practical applications.

3.3. Pressure and object sensing applications

Saraf et al. combined the ferroelectric and semiconducting nature of $MAPbI_3$ to fabricate a light-harvesting, self-powered tactile sensor capable of operating for at least 72h after poling under visible light illumination (Figure 15h-i).[131] The sensor decoupled the energy harvesting and pressure sensing and exhibited a linear response until 76 kPa with a pressure sensitivity of $0.57 kPa^{-1}$. This device could be interesting for remote wearable sensing or continuous monitoring applications. However, by direct piezoelectric force microscopy, Andrés et al. observed ferroelectricity-free in $MAPbI_3$, which is indendent of the grain size, film thickness, grain texture, and electron or hole selective contacts beneath.[152] More detailed studies are needed to fully understand the underlying mechanisms in such sensors. For the first time, Wang et al. proposed a novel perovskite microlaser for detecting nanoscale

objects whose sizes can be measured by the intensity of scattered laser light.[153] One year later, the same groups proposed waveguide devices integrating $MAPbX_3$ perovskite with Si_3N_4 to obtain an on-chip-integrated optical sensor.[154] For the first time, a laser diode like sensor is capable of detecting nanoparticles of radius ≈70 nm. The high sensitivity of perovskite photodetectors can bring benefits like decreased photocurrent and sensing of nanoscale objects. The concept could be applied to any electrically driven microlasers and find applications in portable point-of-care devices.

4. Conclusion

Since the first publication of halide perovskite-based solar cell in 2009, perovskite materials have achieved significant development in the field of optoelectronics due to their excellent optical and electrical properties. Perovskite polycrystalline films are convenient to fabricate, but the grain morphology, grain boundaries, and surface defects all have profound effects on the application in photodetectors and sensors. By contrast, single crystals have low trap state densities and are favorable in detecting weak light as low as pW cm^{-2}. For photodetectors, different mechanisms and structures lead to different performances and particular applications. The photoconductive-type detector has higher responsivity due to its intrinsic gain mechanism. Meanwhile, although a photovoltaic-type detector demonstrates low responsivity, devices with such a structure can suppress the dark current through the transporting layers and barrier layers. On the other hand, due to the shorter diffusion length needed for the carriers, a high response rate can be achieved. It is interesting to investigate another lateral structure, i.e., FET-type detector, which combines the high responsivity of the photoconductive-type detector and low dark current of the photovoltaic-type detector. Besides, halide perovskites can also be used to detect alpha particles, X-rays, and gamma rays and further be used as image sensors. Taking the disadvantages of hybrid perovskites such as instability to water, oxygen, and temperature, in turn, the 'soft' material has advantages in the sensor field with reversible or irreversible sensing performance.

In general, perovskite photodetectors and/or sensors showed unique advantages in production cost, detection performance, and displayed unprecedented development. However, there are challenges in lab-to-fab transition due to the stability concerns of the material and reliability of the devices. Researchers have proposed strategies to tackle the stability issues, such as adding buffer layers, controlling the crystal morphology, passivating the surface defects, and making perovskite-polymer composites, etc. In particular, it is more important to solve the inherent stability problem through strategies like mixing cation (FA^+, MA^+, Cs^+, Rb^+) and anion (Br^-, I^-, Cl^-), using bulky cations to form 2D perovskite, etc. Besides, perovskites typically have low responsivity at the NIR region, a problem that can only be solved by combining another material that is optically active through NIR. In the future, we rationalize several vital aspects that should be focused on: (1) the problem of stability, which could be solved by the interface and compositional engineering or encapsulation; (2) hybrid photodetector that combines several materials to extend the response range and increases the responsivity in the NIR region; (3) the development of flexible detector and sensor, which is very important for the application in electronic smart skin; (4) the development of self-powered photodetectors and sensors that do not or need only low external power support, for the expedient development of the internet of things (IoT). We need more efforts to challenge these problems and enrich this exciting field of perovskite-based optoelectronic devices. It is believed that stable and reliable perovskite photodetectors and sensors will play a critical role in the future.

Acknowledgments

P. Gao knowledge 'the National Natural Science Foundation of China (Grant No. 21975260) and the Recruitment Program of Global Experts of China'.

Received: ((will be filled in by the editorial staff))
Revised: ((will be filled in by the editorial staff))
Published online: ((will be filled in by the editorial staff))

References

[1] A. Kojima, K. Teshima, Y. Shirai, T. Miyasaka, *J. Am. Chem. Soc.* **2009**, *131*, 6050.

[2] P. Gao, M. Grätzel, M. K. Nazeeruddin, *Energy Environ. Sci.* **2014**, *7*, 2448.

[3] "Best Research-Cell Efficiency Chart | Photovoltaic Research | NREL," **n.d.**

[4] S. Shi, Y. Li, X. Li, H. Wang, *Mater. Horizons* **2015**, *2*, 378.

[5] Y. Zhang, F. Fadaei Tirani, P. Pattison, K. Schenk-Joß, Z. Xiao, M. K. Nazeeruddin, P. Gao, *Dalt. Trans.* **2020**, *49*, 5815.

[6] L. Dou, A. B. Wong, Y. Yu, M. Lai, N. Kornienko, S. W. Eaton, A. Fu, C. G. Bischak, J. Ma, T. Ding, N. S. Ginsberg, L. W. Wang, A. P. Alivisatos, P. Yang, *Science (80-.).* **2015**, *349*, 1518.

[7] P. Gao, A. R. Bin Mohd Yusoff, M. K. Nazeeruddin, *Nat. Commun.* **2018**, *9*, 5028.

[8] B. Wang, J. Iocozzia, M. Zhang, M. Ye, S. Yan, H. Jin, S. Wang, Z. Zou, Z. Lin, *Chem. Soc. Rev.* **2019**, *48*, 4854.

[9] Z. Zhao, F. Gu, H. Rao, S. Ye, Z. Liu, Z. Bian, C. Huang, *Adv. Energy Mater.* **2019**, *9*, 1802671.

[10] J. Shi, Y. Gao, X. Gao, Y. Zhang, J. Zhang, X. Jing, M. Shao, *Adv. Mater.* **2019**, *31*, 1901673.

[11] Z. Tan, Y. Wu, H. Hong, J. Yin, J. Zhang, L. Lin, M. Wang, X. Sun, L. Sun, Y. Huang, K. Liu, Z. Liu, H. Peng, *J. Am. Chem. Soc.* **2016**, *138*, 16612.

[12] T. Zhang, F. Wang, P. Zhang, Y. Wang, H. Chen, J. Li, J. Wu, L. Chen, Z. D. Chen, S. Li, *Nanoscale* **2019**, *11*, 2871.

[13] N. G. Park, *Mater. Today* **2015**, *18*, 65.

[14] W. Nie, H. Tsai, R. Asadpour, J. C. Blancon, A. J. Neukirch, G. Gupta, J. J. Crochet, M. Chhowalla, S. Tretiak, M. A. Alam, H. L. Wang, A. D. Mohite, *Science (80-.).* **2015**, *347*, 522.

[15] M. Saliba, T. Matsui, K. Domanski, J.-Y. Seo, A. Ummadisingu, S. M. Zakeeruddin, J.-P. Correa-Baena, W. R. Tress, A. Abate, A. Hagfeldt, M. Gratzel, *Science (80-.).* **2016**, *354*, 206.

[16] W. S. Yang, B.-W. Park, E. H. Jung, N. J. Jeon, Y. C. Kim, D. U. Lee, S. S. Shin, J. Seo, E. K. Kim, J. H. Noh, S. Il Seok, *Science (80-.).* **2017**, *356*, 1376.

[17] Z.-K. Tan, R. S. Moghaddam, M. L. Lai, P. Docampo, R. Higler, F. Deschler, M. Price, A. Sadhanala, L. M. Pazos, D. Credgington, F. Hanusch, T. Bein, H. J. Snaith, R. H. Friend, *Nat. Nanotechnol.* **2014**, *9*, 687.

[18] H. Cho, S.-H. Jeong, M.-H. Park, Y.-H. Kim, C. Wolf, C.-L. Lee, J. H. Heo, A. Sadhanala, N. Myoung, S. Yoo, S. H. Im, R. H. Friend, T.-W. Lee, *Science (80-.).* **2015**, *350*, 1222.

[19] Y. H. Kim, H. Cho, J. H. Heo, T. S. Kim, N. S. Myoung, C. L. Lee, S. H. Im, T. W. Lee, *Adv. Mater.* **2015**, *27*, 1248.

[20] S. D. Stranks, H. J. Snaith, *Nat. Nanotechnol.* **2015**, *10*, 391.

[21] H. Zhu, Y. Fu, F. Meng, X. Wu, Z. Gong, Q. Ding, M. V. Gustafsson, M. T. Trinh, S. Jin, X.-Y. Zhu, *Nat. Mater.* **2015**, *14*, 636.

[22] G. Xing, N. Mathews, S. S. Lim, N. Yantara, X. Liu, D. Sabba, M. Grätzel, S. Mhaisalkar, T. C. Sum, *Nat. Mater.* **2014**, *13*, 476.

[23] Y. Xu, Q. Chen, C. Zhang, R. Wang, H. Wu, X. Zhang, G. Xing, W. W. Yu, X. Wang, Y. Zhang, M. Xiao, *J. Am. Chem. Soc.* **2016**, *138*, 3761.

[24] T. Wu, W. Pisula, M. Y. A. Rashid, P. Gao, *Adv. Electron. Mater.* **2019**, *5*, 1900444.

[25] T. Wu, P. Gao, *Materials (Basel).* **2018**, *11*, 999.

[26] Q. Lin, A. Armin, D. M. Lyons, P. L. Burn, P. Meredith, *Adv. Mater.* **2015**, *27*, 2060.

[27] T. Gao, Q. Zhang, J. Chen, X. Xiong, T. Zhai, *Adv. Opt. Mater.* **2017**, *5*, 1700206.

[28] X. Liu, D. Yu, F. Cao, X. Li, J. Ji, J. Chen, X. Song, H. Zeng, *Small* **2017**, *13*, 1700364.

[29] Z. Hong, W.-H. Chang, G. Li, J. You, L. Dou, Y. Yang, *Nat. Commun.* **2014**, *5*, 1.

[30] S. Ruan, J. Lu, N. Pai, H. Ebendorff-Heidepriem, Y.-B. Cheng, Y. Ruan, C. R. McNeill, *J. Mater. Chem. C* **2018**, *6*, 6988.

[31] Y. Zhang, X. Wang, H. Xiao, Y. Chen, H. Zhong, R. Zhu, X. Li, *J. Phys. Chem. Solids* **2019**, *129*, 270.

[32] D. Zhang, Y. Xu, Q. Liu, Z. Xia, *Inorg. Chem.* **2018**, *57*, 4613.

[33] H. Chen, M. Zhang, R. Bo, C. Barugkin, J. Zheng, Q. Ma, S. Huang, A. W. Y. Ho-Baillie, K. R. Catchpole, A. Tricoli, *Small* **2018**, *14*, 1702571.

[34] L. Su, Z. X. Zhao, H. Y. Li, J. Yuan, Z. L. Wang, G. Z. Cao, G. Zhu, *ACS Nano* **2015**, *9*, 11310.

[35] L. Etgar, P. Gao, P. Qin, M. Graetzel, M. K. Nazeeruddin, *J. Mater. Chem. A* **2014**, *2*, 11586.

[36] S. D. Stranks, G. E. Eperon, G. Grancini, C. Menelaou, M. J. P. P. Alcocer, T. Leijtens, L. M. Herz, A. Petrozza, H. J. Snaith, *Science (80-.).* **2013**, *342*, 341.

[37] D. W. de Quilettes, S. M. Vorpahl, S. D. Stranks, H. Nagaoka, G. E. Eperon, M. E. Ziffer, H. J. Snaith, D. S. Ginger, *Science (80-.).* **2015**, *348*, 683.

[38] C. C. Stoumpos, C. D. Malliakas, M. G. Kanatzidis, *Inorg. Chem.* **2013**, *52*, 9019.

[39] W. J. Yin, T. Shi, Y. Yan, *J. Phys. Chem. C* **2015**, *119*, 5253.

[40] M. A. Green, A. Ho-Baillie, H. J. Snaith, *Nat. Photonics* **2014**, *8*, 506.

[41] L. Meng, Z. Wei, T. Zuo, P. Gao, *Nano Energy* **2020**, *75*, 104866.

[42] L. Liang, H. Luo, J. Hu, H. Li, P. Gao, *Adv. Energy Mater.* **2020**, *10*, 1.

[43] H.-R. Xia, J. Li, W.-T. Sun, L.-M. Peng, *Chem. Commun.* **2014**, *50*, 13695.

[44] Y. Lin, G. Lin, B. Sun, X. Guo, *Adv. Funct. Mater.* **2018**, *28*, 1705589.

[45] J. Miao, F. Zhang, *J. Mater. Chem. C* **2019**, *7*, 1741.

[46] W. Tian, H. Zhou, L. Li, *Small* **2017**, *13*, 1702107.

[47] H. Kim, J. S. Han, J. Choi, S. Y. Kim, H. W. Jang, *Small Methods* **2018**, *2*, 1700310.

[48] F. Mei, D. Sun, S. Mei, J. Feng, Y. Zhou, J. Xu, X. Xiao, *Adv. Phys. X* **2019**, *4*, 1592709.

[49] M. Ahmadi, T. Wu, B. Hu, *Adv. Mater.* **2017**, *29*, 1605242.

[50] K. Domanski, W. Tress, T. Moehl, M. Saliba, M. K. Nazeeruddin, M. Grätzel, *Adv. Funct. Mater.* **2015**, *25*, 6936.

[51] J. Li, L. Niu, Z. Zheng, F. Yan, *Adv. Mater.* **2014**, *26*, 5239.

[52] M. I. Saidaminov, V. Adinolfi, R. Comin, A. L. Abdelhady, W. Peng, I. Dursun, M. Yuan, S. Hoogland, E. H. Sargent, O. M. Bakr, *Nat. Commun.* **2015**, *6*, 8724.

[53] D. N. Dirin, I. Cherniukh, S. Yakunin, Y. Shynkarenko, M. V. Kovalenko, *Chem. Mater.* **2016**, *28*, 8470.

[54] X.-W. Tong, W.-Y. Kong, Y.-Y. Wang, J.-M. Zhu, L.-B. Luo, Z.-H. Wang, *ACS Appl. Mater. Interfaces* **2017**, *9*, 18977.

[55] P. Gui, Z. Chen, B. Li, F. Yao, X. Zheng, Q. Lin, G. Fang, *ACS Photonics* **2018**, *5*, 2113.

[56] S. Chen, C. Teng, M. Zhang, Y. Li, D. Xie, G. Shi, *Adv. Mater.* **2016**, *28*, 5969.

[57] Y. Liu, F. Li, C. Perumal Veeramalai, W. Chen, T. Guo, C. Wu, T. W. Kim, *ACS Appl. Mater. Interfaces* **2017**, *9*, 11662.

[58] H. Deng, X. Yang, D. Dong, B. Li, D. Yang, S. Yuan, K. Qiao, Y.-B. Cheng, J. Tang, H. Song, *Nano Lett.* **2015**, *15*, 7963.

[59] Y. Zhang, Y. Liu, Z. Xu, H. Ye, Q. Li, M. Hu, Z. Yang, S. (Frank) Liu, *J. Mater. Chem. C* **2019**, *7*, 1584.

[60] S.-F. Leung, K.-T. Ho, P.-K. Kung, V. K. S. Hsiao, H. N. Alshareef, Z. L. Wang, J.-H. He, *Adv. Mater.* **2018**, *30*, 1704611.

[61] H. Lu, W. Tian, F. Cao, Y. Ma, B. Gu, L. Li, *Adv. Funct. Mater.* **2016**, *26*, 1296.

[62] Z.-X. Zhang, C. Li, Y. Lu, X.-W. Tong, F.-X. Liang, X.-Y. Zhao, D. Wu, C. Xie, L.-B. Luo, *J. Phys. Chem. Lett.* **2019**, *10*, 5343.

[63] N. Alwadai, M. A. Haque, S. Mitra, T. Flemban, Y. Pak, T. Wu, I. Roqan, *ACS Appl. Mater. Interfaces* **2017**, *9*, 37832.

[64] Y. Zhan, Y. Y. Wang, Q. Cheng, C. Li, K. Li, H. Li, J. Peng, B. Lu, Y. Y. Wang, Y. Song, L. Jiang, M. Li, *Angew. Chemie Int. Ed.* **2019**, *58*, 16456.

[65] C. Perumal Veeramalai, S. Yang, J. Wei, M. Sulaman, R. Zhi, M. I. Saleem, Y. Tang, Y. Jiang, B. Zou, *ACS Appl. Nano Mater.* **2020**, *3*, 459.

[66] C. Bao, Z. Chen, Y. Fang, H. Wei, Y. Deng, X. Xiao, L. Li, J. Huang, *Adv. Mater.* **2017**, *29*, 1703209.

[67] H. L. Zhu, J. Cheng, D. Zhang, C. Liang, C. J. Reckmeier, H. Huang, A. L. Rogach, W. C. H. Choy, *ACS Nano* **2016**, *10*, 6808.

[68] G. Tong, X. Geng, Y. Yu, L. Yu, J. Xu, Y. Jiang, Y. Sheng, Y. Shi, K. Chen, *RSC Adv.* **2017**, *7*, 18224.

[69] B. R. Sutherland, A. K. Johnston, A. H. Ip, J. Xu, V. Adinolfi, P. Kanjanaboos, E. H. Sargent, *ACS Photonics* **2015**, *2*, 1117.

[70] H.-W. Chen, N. Sakai, A. K. Jena, Y. Sanehira, M. Ikegami, K.-C. Ho, T. Miyasaka, *J. Phys. Chem. Lett.* **2015**, *6*, 1773.

[71] Z. Song, H. Zhou, P. Gui, X. Yang, R. Liu, G. Ma, H. Wang, G. Fang, *J. Mater. Chem. C* **2018**, *6*, 5113.

[72] Y. Wang, C. Chen, T. Zou, L. Yan, C. Liu, X. Du, S. Zhang, H. Zhou, *Adv. Mater. Technol.* **2020**, *5*, 1900752.

[73] C. Li, H. Wang, F. Wang, T. Li, M. Xu, H. Wang, Z. Wang, X. Zhan, W. Hu, L. Shen, *Light Sci. Appl.* **2020**, *9*, 31.

[74] C. Bao, W. Xu, J. Yang, S. Bai, P. Teng, Y. Yang, J. Wang, N. Zhao, W. Zhang, W. Huang, F. Gao, *Nat. Electron.* **2020**, *3*, 156.

[75] Y. Cheng, Z. Shi, S. Yin, Y. Li, S. Li, W. Liang, D. Wu, Y. Tian, X. Li, *Sol. Energy Mater. Sol. Cells* **2020**, *204*, 110230.

[76] H. L. Zhu, H. Lin, Z. Song, Z. Wang, F. Ye, H. Zhang, W.-J. Yin, Y. Yan, W. C. H. Choy, *ACS Nano* **2019**, *13*, 11800.

[77] H. Sun, W. Tian, F. Cao, J. Xiong, L. Li, *Adv. Mater.* **2018**, *30*, 1706986.

[78] V. Q. Dang, G.-S. S. Han, T. Q. Trung, L. T. Duy, Y.-U. U. Jin, B.-U. U. Hwang, H.-S. S. Jung, N.-E. E. Lee, *Carbon N. Y.* **2016**, *105*, 353.

[79] C. Chen, X. Zhang, G. Wu, H. Li, H. Chen, *Adv. Opt. Mater.* **2017**, *5*, 1600539.

[80] Z. Liu, Y. Zhu, J. K. El-Demellawi, D. B. Velusamy, A. M. El-Zohry, O. M. Bakr, O. F. Mohammed, H. N. Alshareef, *ACS Energy Lett.* **2019**, *4*, 2315.

[81] H. Wang, R. Haroldson, B. Balachandran, A. A. Zakhidov, S. Sohal, J. Y. Chan, A. A. Zakhidov, W. Hu, *ACS Nano* **2016**, *10*, 10921.

[82] J.-Y. Zhang, J.-L. Xu, T. Chen, X. Gao, S.-D. Wang, *ACS Appl. Mater. Interfaces* **2019**, *11*, 44430.

[83] J. Liu, Y. Xue, Z. Wang, Z. Q. Xu, C. Zheng, B. Weber, J. Song, Y. Wang, Y. Lu, Y. Zhang, Q. Bao, *ACS Nano* **2016**, *10*, 3536.

[84] Z. Yang, J. Dou, M. Wang, J. Li, J. Huang, J. Shao, *J. Mater. Chem. C* **2018**, *6*, 6739.

[85] Y. Wang, X. Zhang, D. Wang, X. Li, J. Meng, J. You, Z. Yin, J. Wu, *ACS Appl. Mater. Interfaces* **2019**, *11*, 28005.

[86] Y. Guo, C. Liu, H. Tanaka, E. Nakamura, *J. Phys. Chem. Lett.* **2015**, *6*, 535.

[87] L. Zeng, Q. Chen, Z. Zhang, D. Wu, H. Yuan, Y. Li, W. Qarony, S. P. Lau, L. Luo, Y. H. Tsang, *Adv. Sci.* **2019**, *6*, 1901134.

[88] W. Deng, L. Huang, X. Xu, X. Zhang, X. Jin, S.-T. Lee, J. Jie, *Nano Lett.* **2017**, *17*, 2482.

[89] Y. Yu, Y. Zhang, Z. Zhang, H. Zhang, X. Song, M. Cao, Y. Che, H. Dai, J. Yang, J. Wang, H. Zhang, J. Yao, *J. Phys. Chem. Lett.* **2017**, *8*, 445.

[90] L. Wu, L. Qin, Y. Zhang, M. Alamri, M. Gong, W. Zhang, D. Zhang, W.-L. Chan, J. Z. Wu, *ACS Appl. Mater. Interfaces* **2018**, *10*, 12824.

[91] H. Wang, D. H. Kim, *Chem. Soc. Rev.* **2017**, *46*, 5204.

[92] G. Konstantatos, E. H. Sargent, *Nat. Publ. Gr.* **2010**, *5*, 391.

[93] X. Hu, X. Zhang, L. Liang, J. Bao, S. Li, W. Yang, Y. Xie, *Adv. Funct. Mater.* **2014**, *24*, 7373.

[94] J. Zhou, Y. Chu, J. Huang, *ACS Appl. Mater. Interfaces* **2016**, *8*, 25660.

[95] D. Shi, V. Adinolfi, R. Comin, M. Yuan, E. Alarousu, A. Buin, Y. Chen, S. Hoogland, A. Rothenberger, K. Katsiev, Y. Losovyj, X. Zhang, P. A. Dowben, O. F. Mohammed, E. H. Sargent, O. M. Bakr, *Science (80-.).* **2015**, *347*, 519.

[96] Q. Dong, Y. Fang, Y. Shao, P. Mulligan, J. Qiu, L. Cao, J. Huang, *Science (80-.).* **2015**, *347*, 967.

[97] S. Li, Y. Xu, C. Li, Q. Guo, G. Wang, H. Xia, H. Fang, L. Shen, H. Sun, *Adv. Mater.* **2020**, *32*, 2001998.

[98] F. Li, C. Ma, H. Wang, W. Hu, W. Yu, A. D. Sheikh, T. Wu, *Nat. Commun.* **2015**, *6*, 1.

[99] I. Khrapach, F. Withers, T. H. Bointon, D. K. Polyushkin, W. L. Barnes, S. Russo, M. F. Craciun, *Adv. Mater.* **2012**, *24*, 2844.

[100] C. Lee, X. Wei, J. W. Kysar, J. Hone, *Science (80-.).* **2008**, *321*, 385.

[101] Y. Lee, J. Kwon, E. Hwang, C.-H. Ra, W. J. Yoo, J.-H. Ahn, J. H. Park, J. H. Cho, *Adv. Mater.* **2015**, *27*, 41.

[102] L. Qin, L. Wu, B. Kattel, C. Li, Y. Zhang, Y. Hou, J. Wu, W.-L. Chan, *Adv. Funct. Mater.* **2017**, *27*, 1704173.

[103] C. Liu, K. Wang, C. Yi, X. Shi, P. Du, A. W. Smith, A. Karim, X. Gong, *J. Mater. Chem. C* **2015**, *3*, 6600.

[104] Y. Fang, J. Huang, *Adv. Mater.* **2015**, *27*, 2804.

[105] L. Shen, Y. Fang, D. Wang, Y. Bai, Y. Deng, M. Wang, Y. Lu, J. Huang, *Adv. Mater.* **2016**, *28*, 10794.

[106] L. Shen, Y. Lin, C. Bao, Y. Bai, Y. Deng, M. Wang, T. Li, Y. Lu, A. Gruverman, W. Li, J. Huang, *Mater. Horizons* **2017**, *4*, 242.

[107] H. L. Zhu, Z. Liang, Z. Huo, W. K. Ng, J. Mao, K. S. Wong, W. J. Yin, W. C. H. Choy, *Adv. Funct. Mater.* **2018**, *28*, 1706068.

[108] W. Wang, D. Zhao, F. Zhang, L. Li, M. Du, C. Wang, Y. Yu, Q. Huang, M. Zhang, L. Li, J. Miao, Z. Lou, G. Shen, Y. Fang, Y. Yan, *Adv. Funct. Mater.* **2017**, *27*, 1703953.

[109] Z. Chen, C. Li, A. A. Zhumekenov, X. Zheng, C. Yang, H. Yang, Y. He, B. Turedi, O. F. Mohammed, L. Shen, O. M. Bakr, *Adv. Opt. Mater.* **2019**, *7*, 1900506.

[110] M. I. Saidaminov, M. A. Haque, M. Savoie, A. L. Abdelhady, N. Cho, I. Dursun, U. Buttner, E. Alarousu, T. Wu, O. M. Bakr, *Adv. Mater.* **2016**, *28*, 8144.

[111] H.-S. Rao, W.-G. Li, B.-X. Chen, D.-B. Kuang, C.-Y. Su, *Adv. Mater.* **2017**, *29*, 1602639.

[112] L. Li, Y. Deng, C. Bao, Y. Fang, H. Wei, S. Tang, F. Zhang, J. Huang, *Adv. Opt. Mater.* **2017**, *5*, 1700672.

[113] X. Wu, B. Zhou, J. Zhou, Y. Chen, Y. Chu, J. Huang, *Small* **2018**, *14*, 1800527.

[114] H. Sun, W. Tian, X. Wang, K. Deng, J. Xiong, L. Li, *Adv. Mater.* **2020**, *32*, 1908108.

[115] S. Chen, C. Teng, M. Zhang, Y. Li, D. Xie, G. Shi, *Adv. Mater.* **2016**, *28*, 5969.

[116] J. Li, Y. Shen, Y. Liu, F. Shi, X. Ren, T. Niu, K. Zhao, S. F. Liu, *ACS Appl. Mater. Interfaces* **2017**, *9*, 19176.

[117] Q. Lin, A. Armin, P. L. Burn, P. Meredith, *Laser Photon. Rev.* **2016**, *10*, 1047.

[118] Y. Li, Y. Zhang, T. Li, M. Li, Z. Chen, Q. Li, H. Zhao, Q. Sheng, W. Shi, J. Yao, *Nano Lett.* **2020**, acs. nanolett.0c00082.

[119] Q. Xu, H. Wei, W. Wei, W. Chuirazzi, D. Desantis, J. Huang, *Nucl. Inst. Methods Phys. Res. A* **2017**, *848*, 106.

[120] S. Yakunin, D. N. Dirin, Y. Shynkarenko, V. Morad, I. Cherniukh, O. Nazarenko, D. Kreil, T. Nauser, M. V Kovalenko, *Nat. Photonics* **2016**, *10*, 585.

[121] H. Wei, D. DeSantis, W. Wei, Y. Deng, D. Guo, T. J. Savenije, L. Cao, J. Huang, *Nat. Mater.* **2017**, *16*, 826.

[122] H. Wei, Y. Fang, P. Mulligan, W. Chuirazzi, H. Fang, C. Wang, B. R. Ecker, Y. Gao, M. A. Loi, L. Cao, *Nat. Photonics* **2016**, *10*, 333.

[123] S. Yakunin, M. Sytnyk, D. Kriegner, S. Shrestha, M. Richter, G. J. Matt, H. Azimi, C. J. Brabec, J. Stangl, M. V. Kovalenko, W. Heiss, *Nat. Photonics* **2015**, *9*, 444.

[124] Q. Chen, J. Wu, X. Ou, B. Huang, J. Almutlaq, A. A. Zhumekenov, X. Guan, S. Han, L. Liang, Z. Yi, J. Li, X. Xie, Y. Wang, Y. Li, D. Fan, D. B. L. Teh, A. H. All, O. F. Mohammed, O. M. Bakr, T. Wu, M. Bettinelli, H. Yang, W. Huang, X. Liu, *Nature* **2018**, *561*, 88.

[125] J. T. Tisdale, T. Smith, J. R. Salasin, M. Ahmadi, N. Johnson, A. V Ievlev, M. Koehler, C. J. Rawn, E. Lukosi, B. Hu, *CrystEngComm* **2018**, *20*, 7818.

[126] W. Wei, Y. Zhang, Q. Xu, H. Wei, Y. Fang, Q. Wang, Y. Deng, T. Li, A. Gruverman, L. Cao, J. Huang, *Nat. Photonics* **2017**, *11*, 315.

[127] L. Gu, M. M. Tavakoli, D. Zhang, Q. Zhang, A. Waleed, Y. Xiao, K.-H. Tsui, Y. Lin, L. Liao, J. Wang, Z. Fan, *Adv. Mater.* **2016**, *28*, 9713.

[128] J. H. Kim, S. H. Kim, *Dye. Pigment.* **2016**, *134*, 198.

[129] W. Xu, F. Li, Z. Cai, Y. Wang, F. Luo, X. Chen, *J. Mater. Chem. C* **2016**, *4*, 9651.

[130] Y. Niu, F. Zhang, Z. Bai, Y. Dong, J. Yang, R. Liu, B. Zou, J. Li, H. Zhong, *Adv. Opt. Mater.* **2015**, *3*, 112.

[131] R. Saraf, L. Pu, V. Maheshwari, *Adv. Mater.* **2018**, *30*, 1705778.

[132] S. H. Kim, A. Kirakosyan, J. Choi, J. H. Kim, *Dye. Pigment.* **2017**, *147*, 1.

[133] X. Chen, H. Hu, Z. Xia, W. Gao, W. Gou, Y. Qu, Y. Ma, *J. Mater. Chem. C* **2017**, *5*, 309.

[134] P. Wu, Q. He, D. Zhu, H. Jiang, Z. Jiao, Y. Zhang, W. Xu, Y. Fu, H. Cao, J. Cheng, *Anal. Methods* **2017**, *9*, 3804.

[135] Y. Zhuang, W. Yuan, L. Qian, S. Chen, G. Shi, *Phys. Chem. Chem. Phys.* **2017**, *19*, 12876.

[136] M. Zhu, L. Zhang, J. Yin, J. Chen, L. Bie, B. D. Fahlman, *Sensors Actuators B. Chem.* **2019**, *282*, 659.

[137] X. You, J. Wu, Y. Chi, *Anal. Chem.* **2019**, *91*, 5058.

[138] G. Kakavelakis, E. Gagaoudakis, K. Petridis, V. Petromichelaki, V. Binas, G. Kiriakidis, E. Kymakis, *ACS Sensors* **2018**, *3*, 135.

[139] F. Lin, F. Li, Z. Lai, Z. Cai, Y. Wang, O. S. Wolfbeis, X. Chen, *ACS Appl. Mater. Interfaces* **2018**, *10*, 23335.

[140] Y. Chen, X. Zhang, Z. Liu, Z. Zeng, H. Zhao, X. Wang, J. Xu, *Microchim. Acta* **2019**, *186*, 47.

[141] Y. Wang, Y. Zhu, J. Huang, J. Cai, J. Zhu, X. Yang, J. Shen, H. Jiang, C. Li, *J. Phys. Chem. Lett.* **2016**, *7*, 4253.

[142] J. Qin, S. Cui, X. Yang, G. Yang, Y. Zhu, Y. Wang, D. Qiu, *J. Phys. D. Appl. Phys.* **2019**, *52*, 415101.

[143] X. Shan, S. Zhang, M. Zhou, T. Geske, M. Davis, A. Hao, H. Wang, Z. Yu, *Adv. Mater. Interfaces* **2019**, *6*, 1.

[144] K. Ren, L. Huang, S. Yue, S. Lu, K. Liu, M. Azam, Z. Wang, Z. Wei, S. Qu, Z. Wang, *J. Mater. Chem. C* **2017**, *5*, 2504.

[145] Z. Weng, J. Qin, A. A. Umar, J. Wang, X. Zhang, H. Wang, X. Cui, X. Li, L. Zheng, Y. Zhan, *Adv. Funct. Mater.* **2019**, *29*, 1902234.

[146] Y. Zhu, F. Li, Y. Huang, F. Lin, X. Chen, *Anal. Chem.* **2019**, *91*, 14183.

[147] B. Zhuang, Y. Liu, S. Yuan, H. Huang, J. Chen, D. Chen, *Nanoscale* **2019**, *11*, 15010.

[148] Y. Wang, Y. Zhu, J. Huang, J. Cai, J. Zhu, X. Yang, J. Shen, H. Jiang, C. Li, *J. Phys. Chem. Lett.* **2016**, *7*, 4253.

[149] Y. Wang, Y. Zhu, J. Huang, J. Cai, J. Zhu, X. Yang, J. Shen, C. Li, *Nanoscale Horizons* **2017**, *2*, 225.

[150] L. Lu, T. Tan, X. Tian, Y. Li, P. Deng, *Anal. Chim. Acta* **2017**, *986*, 109.

[151] Y. Liu, X. Tang, T. Zhu, M. Deng, I. P. Ikechukwu, W. Huang, G. Yin, Y. Bai, D. Qu, X. Huang, F. Qiu, *J. Mater. Chem. C* **2018**, *6*, 4793.

[152] A. Gómez, Q. Wang, A. R. Goñi, M. Campoy-Quiles, A. Abate, *Energy Environ. Sci.* **2019**, *12*, 2537.

[153] K. Wang, G. Li, S. Wang, S. Liu, W. Sun, C. Huang, Y. Wang, Q. Song, S. Xiao, *Adv. Mater.* **2018**, *30*, 1801481.

[154] W. Sun, C. Huang, R. Fan, S. Liu, Y. Wang, Y. Xiao, Q. Gan, S. Xiao, Q. Song, *Adv. Opt. Mater.* **2019**, *7*, 1801308.

Xiaoyan Yu received her bachelor degree from Hubei University, china, in 2018. And now, she is studying for her master's degree under the guidance of P.Gao, at Fujian Institute of Research on the Structure of Matter, Chinese Academy of Sciences, China. Her research is aiming at the fabrication of highly-efficient perovskite solar cells and the exploring the application in photo-detecting of perovskites.

Dr. Hoi Nok Tsao is an assistant professor in physics at the Nanyang Technological University Singapore, the National Institute of Education. His research interests lie in the field of organic electronics, optoelectronic devices for computer vision, and unconventional neuromorphic devices for artificial intelligence. Dr. Tsao received his Bachelor's degree in physics at the University of California at Berkeley, followed by a Maters' degree in physics from the Ludwig Maximilians University in Munich, Germany. He completed his Ph.D. in the field of organic field effect transistors at the Max Planck Institute for Polymer Research in Mainz, Germany. Subsequently, he worked on solar cells as a Postdoctorial fellow at the Ecole Polytechnique Federale de Lausanne in Switzerland.

Dr. Peng Gao studied since 2006 as Ph.D. at MPIP (Mainz, Germany) in the group of Prof. Müllen. Since 2010, he joined the lab of Prof. Grätzel at EPFL (Lausanne, Switzerland) as a postdoctoral researcher. From 2015 he worked with Prof. Nazeeruddin at the EPFL Sion Energy Center as a group leader. He started the Laboratory of Advanced Functional Materials (LAFM) in 2017 at Fujian Institute of Research on the Structure of Matter, Chinese

Academy of Science and focus on the application of rare-earth elements in organic optoelectronic and energy conversion materials.

Sensing-behavior: Converting a weak or quantitative signal to a phenomenon visible to the human eye or a specific data is important in the fields of industry and research. Perovskites are applied extensively in photoelectric devices due to the excellent photoelectric properties and solution-fabricated methods with low-cost.

Keywords: perovskites, photodetectors, sensors, imaging, sensitivity

Xiaoyan Yu[1,2,3], Hoi Nok Tsao[4], and Peng Gao[1,2,3*]

Perspicacious and Miscellaneous: Hybrid Halide Perovskite Materials Based Photodetectors and Sensors